Single-Electron Transport in Nanostructured Dirac Materials

K. L. Chiu[1], Yang Xu[2]
[1]*Department of Physics, Massachusetts Institute of Technology, Cambridge, MA 02139, USA and*
[2]*Institute of Microelectronics and Optoelectronics,*
College of Information Science and Electronic Engineering, Zhejiang University, 310027 P. R. China
(Dated: January 7, 2016)

The relativistic dynamics of electronic excitations in two-dimensional Dirac materials such as graphene and the surface states of topological insulators gives rise to superb electronic properties relevant to a wide range of applications and fundamental questions in condensed matter physics. Graphene is a robust material for spintronics owing to its weak spin-orbit and hyperfine interaction, while the surface states of topological insulators exhibit a spin-momentum locking that opens up the possibility for controlling the spin degree of freedom in the absence of external magnetic fields. Nanostructures made of these materials are also viable in quantum computing applications involving the superposition and entanglement of individual charge and spin quanta. In this article, we review recent developments towards confining and manipulating charges in nanostructures fabricated from both graphene and topological insulators. We first focus on transport in graphene nanoribbons and quantum dots fabricated on SiO_2 substrates and more recently on hexagonal boron nitride substrates in order to reduce the bulk disorder. In the second part of this article, we extend our discussion to topological insulators (TIs). After a brief review of bulk TI properties, we review recent developments in the fabrication and understanding of electronic properties of TI nanostructures. Finally, we outline how future work geared towards developing qubits in Dirac materials.

1. INTRODUCTION

Since the 1960s, the density of components on Silicon chips has doubled every 18 months or so, a trend named Moore's law after the prediction from Intel's cofounder Gordon Moore. Silicon-based transistor manufacturing has now reached the sub-10nm scale, heralding the limit of Moore's law and stimulating the development of alternative switching technologies and host materials for processing and storing bits of information. Quantum bits, or 'qubits', are at the heart of quantum computing, an entirely different paradigm which encodes information using superposition states of individual quanta. Ideally, one wishes to use a single electron transistor (SET) or quantum dot (QD) to manipulate single electron spin as a building block for more complicated computing devices. In order to reach this goal, tremendous efforts have been poured into studying the transport properties of QDs made from semiconductors such as GaAs and silicon, and more recently graphene and other 2D materials [1–6]. While the high mobility of GaAs enabled the rapid development of spin qubits [7], the heavy atomic weight of gallium and arsenide atoms limits the spin relaxation time, which makes it less ideal for upscaling. Silicon QDs do not suffer from the heavy atomic weight and have shown a long enough spin relaxation time [8], but the mobility is limited by its doping mechanism. While research on these materials is still ongoing, graphene has attracted significant attention for its relativistic bandstructure and strictly two-dimensional (2D) nature [9]. The weak spin-orbit interaction and hyperfine effect in carbon atoms has made graphene a promising candidate for making spintronic devices and spin qubits [10]. The recent boom in activity focusing on graphene has stimulated interest in many other 2D materials for their distinct bandstructures. These 2D layers can be integrated into lateral or vertical 2D heterostructures, resulting in versatile electronic properties [11]. In particular, hexagonal boron nitride (hBN), an insulator with the same lattice structure as graphene, is an ideal substrate for preserving the high mobility of carriers in pristine graphene [12–16], and can be used as a smooth tunnel barrier for vertical tunneling devices [17–19]. 3D topological insulators exhibit surface states whose excitations share similarities with Dirac fermions in graphene, but with real - rather than pseudo - spin locked to the quasimomentum. They hold promise for dissipationless spintronics and for operating quantum devices in the absence of an external magnetic field [20–22]. In this paper, we review the quantum transport properties of graphene and 3D TI nanodevices. We will start from graphene nanostructures that exhibit QD behavior, such as nanoribbons, single quantum dots and double quantum dots fabricated on Si/SiO_2 substrate. We will then review the more recent progress in which they are fabricated on hBN. In the last part, we will describe nanodevices that are fabricated from topological insulators, such as Bi_2Se_3 nanowires and single quantum dots. Finally, we will address future directions yet to be explored for novel qubits based on 2D Dirac materials.

2. GRAPHENE NANOSTRUCTURES ON SIO_2/SI SUBSTRATE

2.1. Graphene Nanoribbons

Graphene is a monolayer of carbon atoms packed into a two-dimensional honeycomb lattice. Electron dispersion

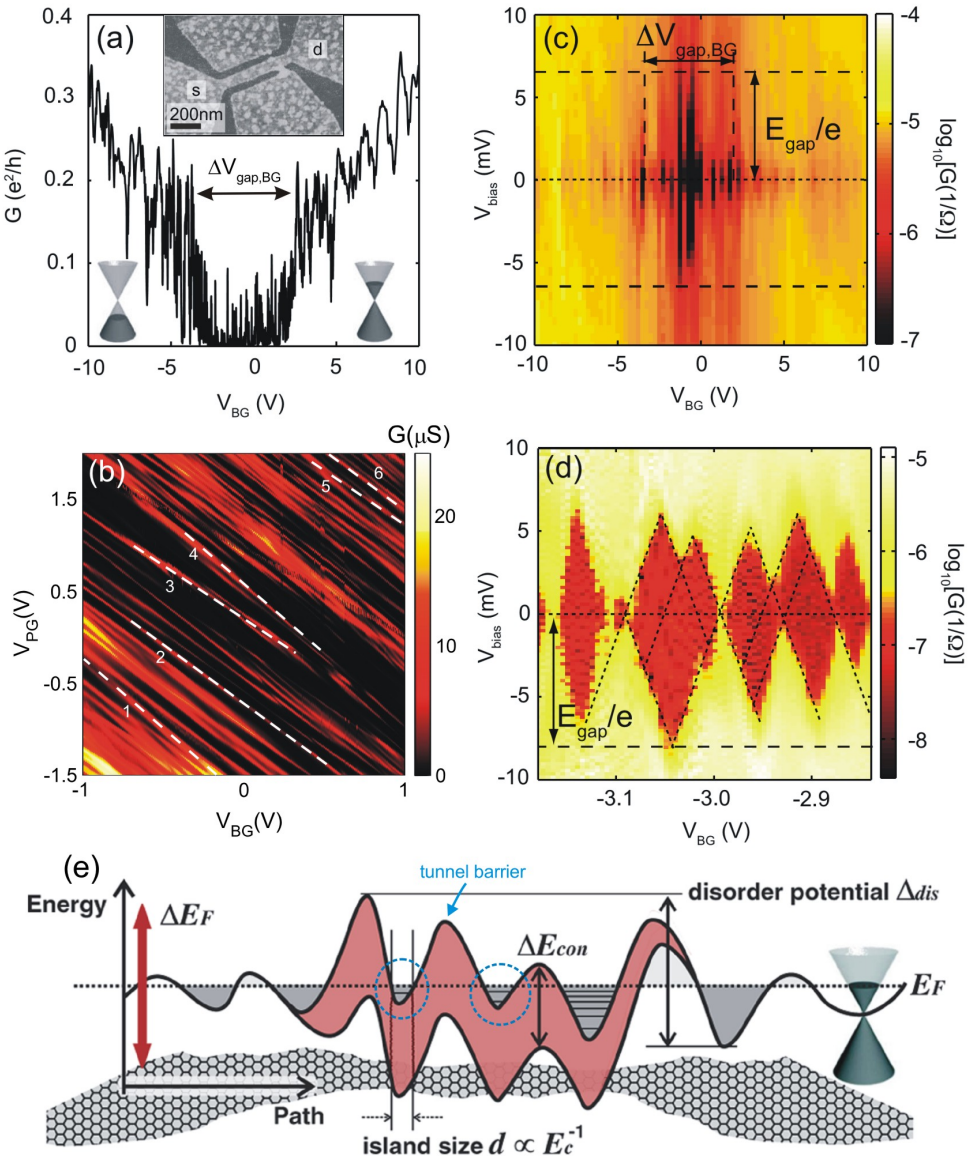

FIG. 1: (a) Conductance through the nanoribbon (shown in insert) as a function of back-gate voltage V_{BG}, recorded with an applied bias voltage V_{bias} = 300 μV and at a temperature T= 2 K. Insert: Atomic Force Microscope image of the graphene nanoribbon (w = 85 nm, l = 500 nm) etched by O_2 plasma. (b) Conductance as a function of V_{BG} and plunger-gate voltage V_{PG} of another GNR device shows a variation in the slope of the Coulomb resonances (indicated by dashed lines and number). (c) Logarithmic conductance as a function of V_{bias} and V_{BG} at T= 2 K of the device shown in (a), with indication of the extent of the transport gap $\Delta V_{gap,BG}$ in back gate and bias gap E_{gap} in bias direction. (d) Zoom-in of the region of suppressed conductance measured in (c). (e) Schematic illustration of the formation of localized states due to disorder. Δ_{dis} characterize the strength of the charge-neutrality point fluctuation and ΔE_{con} is a confinement gap induced by local constriction. ΔE_F denotes the Fermi energy spacing that transport gap has to overcome. (a, c, d) adapted with permission from ref. [23]. (b) reproduced from K. L. Chiu, PhD-Thesis, 2012. (e) adapted with permission from ref. [24]. Copyright 2009 American Physical Society.

of graphene in the low energy regime is linear and gapless, mimicking that of massless Dirac Fermions [25, 26]. The transmission of electrons in graphene is described by a mechanism known as Klein tunneling in which they are less subject to back-scattering by the defect potential, resulting in an excellent conductivity and mobility of graphene field-effect devices [27–29]. While offering advantages for sensing and analog electronics, this gapless bandstructure hinders graphene's application in logic circuits. Owing to the absence of band gap, one cannot completely turn off the current in graphene, leading to on/off ratios that are insufficient for switches [30]. Engineering band gaps in graphene is thus a major challenge in using graphene-based transistors in digital electron-

ics. Theories predict that cutting graphene into one-dimensional nanoribbons can open up a scalable band gap $E_g = \alpha/w$, where w is the nanoribbon width and α is in the range of 0.2 eV·nm to 1.5 eV·nm, depending on the model and the crystallographic orientation of the edges [31, 32]. This stimulated an experimental effort to establish whether nanostructuring graphene is a credible route to opening a band gap. GNRs can be fabricated by O_2 plasma etching using physical masks [23, 33–36], unzipping carbon nanotubes [37–39], gas phase etching [40] and functionalization [41, 42]. These devices were tested at different temperatures for their transport properties and the general results will be discussed below.

Fig. 1(a) shows the conductance of an O_2 plasma etched GNR [inset of Fig. 1(a)] as a function of the voltage applied to the back-gate. This back-gate sweep shows a typical V-shape, with a region around 0 V separating the hole- from electron-transport regime where the conductance is strongly suppressed. In contrast to the prediction of energy gaps in clean GNRs (i.e. without considering bulk disorder and edge roughness), where transport should be completely pinched-off, this gap exhibits a large number of conductance peaks reminiscent of Coulomb blockade resonances in quantum dots. The nature of these resonances can be interrogated by varying the potential of the GNR. Fig. 1(b) shows the conductance as a function of both back-gate and plunger-gate (an in-plane gate close to the GNR) voltage within the transport gap. The conductance resonances exhibit a range of relative lever arms indicated by dashed lines are present over a wide range of V_{BG} and V_{PG} voltage within the gapped region. One explanation for this behavior draws on its similarity to a series of charge islands, each coupled to the plunger-gate through different capacitive coupling strength (assuming the lever arm of the back-gate to the charge islands is nearly constant all over the GNR). More information about such localized states in the GNR can be gleaned by measuring the differential conductance as a function of back-gate voltage and the voltage applied between the source and drain contacts, as can be seen in Fig. 1(c). Within this picture, the extent in bias voltage of the diamond-shaped regions of suppressed current [E_{gap}/e, see Fig. 1(c) and Fig. 1(d)] is a direct indication of the charging energy of the dot, which fluctuates strongly with V_{BG} and extends to ≈ 8.5 meV. The overlapping diamonds in Fig. 1(d) resembles the behavior of a quantum dot network [43], supporting the notion that multiple quantum dots form along the GNR. The gap in Fermi energy ΔE_F corresponding to the transport gap $\Delta V_{gap,BG}$ can be estimated using $\Delta E_F \approx \hbar\nu_F\sqrt{2\pi C_g \Delta V_{gap,BG}/|e|}$, where C_g is the back-gate capacitance per area and ν_F is the Fermi velocity in graphene [24, 44]. This leads to an energy gap $\Delta E_F \approx$ 110-340 meV which is significantly larger than E_{gap} (8.5 meV) and the band gaps $\Delta E_{con} \leq 50$ meV estimated from calculations of a GNR with width $W = 45$ nm [44].

The schematic model shown in Fig. 1(e) is able to qualitatively explain the findings described above [24]. This model consists of a combination of quantum confinement energy gap (ΔE_{con}, the intrinsic band-gap of a clean GNR) and strong bulk and edge-induced disorder potential fluctuation (Δ_{dis}). The confinement energy ΔE_{con} alone can neither explain the observed energy scale ΔE_F, nor the dot formation in the GNR. However, superimposing a fluctuations in the disorder potential can result in the transport blockade between localized states [for example, dashed circles in Fig. 1(e)], in which the tunnel barriers [see blue arrow in Fig. 1(e)] separating different states are defined by the confinement gap. Within this model, ΔE_F depends on both the confinement energy gap and the disorder potential fluctuation and can be approximated using the relation $\Delta E_F = \Delta_{dis} + \Delta E_{con}$. Δ_{dis} can be estimated from the bulk carrier density fluctuations Δn (due to substrate disorder) using $\Delta_{dis} = \hbar\nu_F\sqrt{4\pi\Delta n}$, where $\Delta n \approx \pm 2 \times 10^{11}$ is extracted from ref. [45]. This in turns gives $\Delta E_F = \hbar\nu_F\sqrt{4\pi\Delta n} + \Delta E_{con} \approx 126$ meV [44], which is comparable to the experimental value. The energy gap in the bias direction (E_{gap}) is not directly determined by the strength of ΔE_F but rather by its spatial variation, which results in the charge puddles with different size. One can imagine when the Fermi energy (V_{BG}) lies in the center of the transport gap, the smaller localized states are more likely to form, giving rise to larger charging energy (larger Coulomb diamonds). On the other hand, when the Fermi energy is tuned away from the charge-neutrality point, the size of the relevant diamonds gets generally smaller due to the merging of individual puddles. Although the localized states in graphene constrictions pose additional complications, they can readily be used as tunable tunneling barriers for transport measurements in graphene quantum dots. While a large number of works have been reported in the field on GNRs, in this review we will focus more on the graphene SET using GNRs as tunnel barriers. More information of GNRs can be found in Ref. [46]. In the next section, we will introduce the transport properties of graphene nanstructures made of isolated graphene islands as QDs and GNRs as tunnel barriers.

2.2. Electronic and Magnetic Properties of Graphene Single Quantum Dots

Owing to the expected long spin relaxation time, graphene quantum dots (GQDs) - small islands of confined charge - are considered to be a viable candidate for making spin qubits and spintronic devices [10]. Over the past decade GQDs have proven to be a useful platform for confining and manipulating single electrons [2, 3, 47–52]. GQDs can be formed by etching isolated islands connected to source and drain graphene reservoirs via

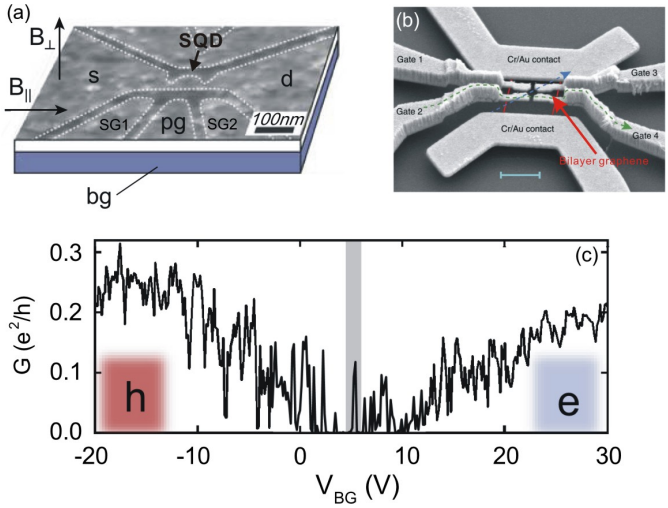

FIG. 2: (a) Atomic Force Microscope image of a graphene single quantum dot ($\approx$ 50 nm wide and $\approx$ 80 nm long) etched by O_2 plasma. (b) Scanning Electron Micrograph of a suspended bilayer GQD device. Bilayer graphene (highlighted by red line) is suspended between two electrodes below local top gates. Scale bar, 1 μm. (c) Source-drain conductance as a function of back-gate voltage V_{BG} at bias V_b = 4 mV measured from the device shown in (a). (a, c) adapted with permission from ref. [3]. Copyright 2009 American Physical Society. (b) adapted with permission from ref. [54]. Copyright 2012 Nature Publishing Group.

nanoconstrictions that are resistive enough to act as tunnel barriers [2, 3, 47]. An example of such a device is shown in Fig. 2(a), in which in-plane graphene side and plunger gates (SG1, SG2, PG) are used to locally tune the potential of the tunnel barriers and the 50 nm diameter dot, while the doped-silicon back-gate (BG) is used to adjust the overall Fermi level. Another way to define a GQD is to induce a band-gap in bilayer graphene by an electric field perpendicular to the layers, in this way charges are confined in an island defined by top gate geometry [53, 54]. Such a structure can be seen in Fig. 2(b), where a bilayer graphene is suspended between two Cr/Au electrodes and sits below suspended local top gates that are used to break interlayer symmetry. Graphene quantum dots can also be formed from the disorder potential [55, 56], strain engineering [57] and gated GNRs [50], in which Coulomb blockade regime can be observed.

Fig. 2(c) shows the back-gate sweep (conductance as a function of back-gate voltage) of the device shown in Fig. 2(a). The measurement shows a transport gap ranging from $0 \leq V_{BG} \leq 10$ V, in which current is suppressed except for multiple sharp Coulomb resonances, separating hole- from electron-transport regime. The transport gap resulting from the GNR tunnel barriers can be lifted using the side-gate voltage. Fig. 3(a) shows the current measurements of another GQD (diameter $\approx$ 180 nm) as a function of its side-gate voltages V_{SG1} and V_{SG2} at a fixed back-gate voltage within the transport gap. There is a cross-like region of suppressed current separating four large conductance regions, which correspond to different doping configurations labeled as NN, NP, PP and PN at the corners of the diagram, respectively. For example, keeping V_{SG1}= -20 V constant and sweeping V_{SG2} from -20 V to +20 V keeps constriction 1 in the p-doped regime whereas constriction 2 is tuned from p-doped to n-doped (PP to PN transition). In order to observe single electron transport, it is necessary to operate in a region of gate space where both tunnel barriers are resistive (i.e., within the center of the cross-like current suppressed regime). Fig. 3(b) shows the case with the Fermi energy located at the edge of the transport gap for both constrictions [marked by the white square in Fig. 3(a)]. The measurement shows broaden vertical and horizontal resonances [white and yellow dashed lines in Fig. 3(b)], which correspond to resonant transmission through the localized states in the left and right constrictions, tuned with the respective side-gate. The fact that those lines are almost perfectly vertical and horizontal indicates that the side-gate only influences the adjacent constriction. A closer inspection of Fig. 3(b) shows a series of diagonal lines (indicated by arrows) which correspond to the Coulomb blockade resonances from the central quantum dot, where both side gates are expected to have a similar lever arm. These 0D Coulomb resonances can be unambiguously resolved as a series of well-defined and regular peaks, as shown in Fig. 3(c), by sweeping a plunger gate voltage V_{PG} with sides gates fixed at V_{SG1} = 5.67 V and V_{SG2} = 2.03 V [the white cross in Fig. 3(b)]. A charge stability measurement of these resonances further confirms their origin, in which a charging energy $E_C \approx 3.2$ meV is extracted from the vertical extent of the Coulomb diamonds shown in Fig. 3(d), in reasonable agreement with the dot diameter [58]. In the following sections, we focus on GQDs whose 0D energy spectrum has been explored in the presence of perpendicular and in-plane magnetic fields.

2.2.1 Electron-hole crossover in perpendicular magnetic field

The energy spectrum of a quantum dot in 2DEG system in the presence of a magnetic field is typically solved using a single particle approximation with a parabolic confinement potential [59, 60]. Such a spectrum is called the Fock-Darwin diagram which describes how 0D levels evolve with respect to an applied perpendicular magnetic field in a radially symmetric quantum dot. In graphene quantum dots, the Fock-Darwin spectrum is notably different compared to the 2DEG case owing to the existence of a Landau level (LL) at zero energy, which does not shift in energy with increasing magnetic field [61, 62]. The unique linear band dispersion of graphene together

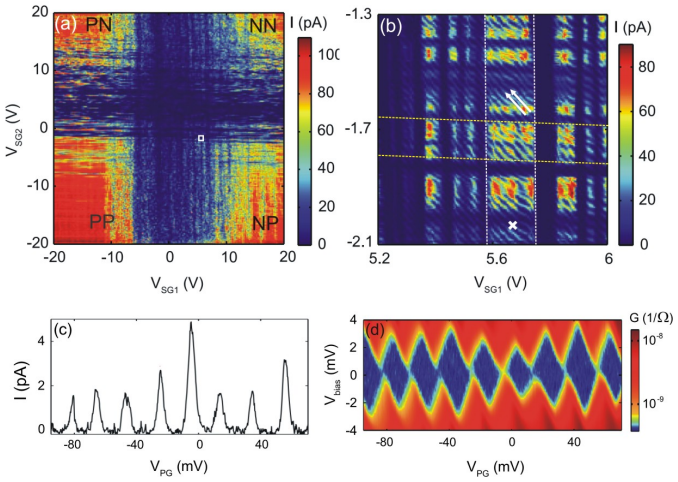

FIG. 3: (a) Current through a GQD (diameter ≈ 180 nm) as a function of two side-gate voltages V_{SG1} and V_{SG2}. (b) Current as a function of V_{SG1} and V_{SG2} in the range indicated by the white square in (a). (c) Current as a function of plunger gate voltage V_{PG} at V_{SG1} = 5.67 V and V_{SG2} = -2.033 V [the white cross in (b)]. (d) Coulomb diamonds associated with the Coulomb resonances in (c). Adapted with permission from ref. [58].

with quantum confinement results in an electron-hole crossover in GQD's magneto-transport [3, 48]. Fig. 4(a) shows a tight-binding simulated Fock-Darwin spectrum of a 50 × 80 nm graphene QD, where a constant charging energy E_C=18 meV have been added to each single-particle level spacing (≈4 meV in average). Several key features seen from the spectrum are summarized in the following. At low B-field, the 0D levels fluctuate but stay at roughly the same energy, as can be seen in the regime I of Fig. 4(a). This fluctuating Coulomb blockade resonances at low B is due to the continuously crossing of different unfilled states with different n and m, where n is the radial quantum number and m is the angular momentum quantum number. This situation changes when the second lowest LL is full, at which point the levels show a kink (regime II) indicating that the electrons (or holes) start to condense into the lowest Landau level (E_0), and the B-field onset of this kink increases with increasing number of particles in the quantum dot. Beyond this B-field, the levels tend to move towards the charge-neutrality point (regime III), meaning the hole levels move to higher energies while the electron levels move to lower energies. At large enough B-field, eventually the levels stop moving and stay roughly at the same energy again (regime IV), indicating the full condensation of electrons/holes into the lowest LL. The Fock-Darwin spectrum of the GQD in Fig. 2(a) has been studied experimentally by tracking the position of Coulomb peaks under the influence of perpendicular magnetic field, as shown in Fig. 4(b). Comparing the numerical data and the measurement [Fig. 4(a) and (b)] one can find the same qualitative trend of states running toward the center (E_0). The arrows in Fig. 4(b) indicate the kinks beyond which all the levels start to fall into the lowest Landau level. These kinks in the magnetic-field dependence of Coulomb resonances can be used to identify the few-carrier regime in graphene quantum dots. The opposite energy shift for electrons and holes in the Fock-Darwin spectrum also provides a method to estimate the charge neutrality point in GQDs [48], but the precise first electron to hole transition is difficult to identify. This can be attributed to the formation of localized states near the Dirac point, which exhibit a weak magnetic-field dependence that alters the spectrum. It is also worth noting that the parasitic magnetic resonances in the tunnel barrier GNRs can also alter the magnetotransport in the GQD [48], which complicates a direct comparison with the simulated Fock-Darwin spectrum.

2.2.2 Zeeman splitting of spin states in in-plane magnetic field

Perpendicular magnetic fields strongly affect the component of the electron wavefunctions in a QD, resulting in the Fock-Darwin spectrum. In-plane magnetic fields, on the other hand, leave the orbital component unaffected, making it possible to explore Zeeman splitting of QD [49, 63, 64]. It is critical to perfectly align the sample plane to the magnetic field to reduce the perpendicular components, which can be technically difficult. However, this problem can be minimized if one can analyze spin pairs, i.e. two subsequently filled electrons occupying the same orbital state with opposite spin orientation. In this case, the orbital contributions can be significantly reduced by subtracting the positions of individual peaks sharing the same orbital shift in perpendicular magnetic field. Potential spin pairs can be identified by tracking the evolution of two subsequent Coulomb peaks with increasing perpendicular magnetic field, as shown in Fig. 5(a). For example, the lowest two peaks (B1 and B2) and the following two (B3 and B4) are identified as potential spin pairs due to their similar peak evolution. Fig. 5(b) shows a measurement of the same peaks in Fig. 5(a) but with increasing in-plane magnetic fields after the sample is carefully rotated into an orientation parallel to the applied B-field. The peaks show a small energy shift with in-plane B-field, indicating the orbital effect is negligible. In order to analyze the movement of the peaks in more details, Fig. 5(c) show the fit of the data selected from Fig. 5(a) and (b), in which two adjacent peaks (a spin pair) are plotted with suitable offsets in V_{pg} such that pairs coincide at B=0 T. As can be seen from the left panel of Fig. 5(c), the orbital states of each pair have approximately the same $B_\perp$ dependence, hence spurious orbital contributions (from slight misalignment) to the peak spacing in $B_{||}$ are limited, resulting in a resolvable

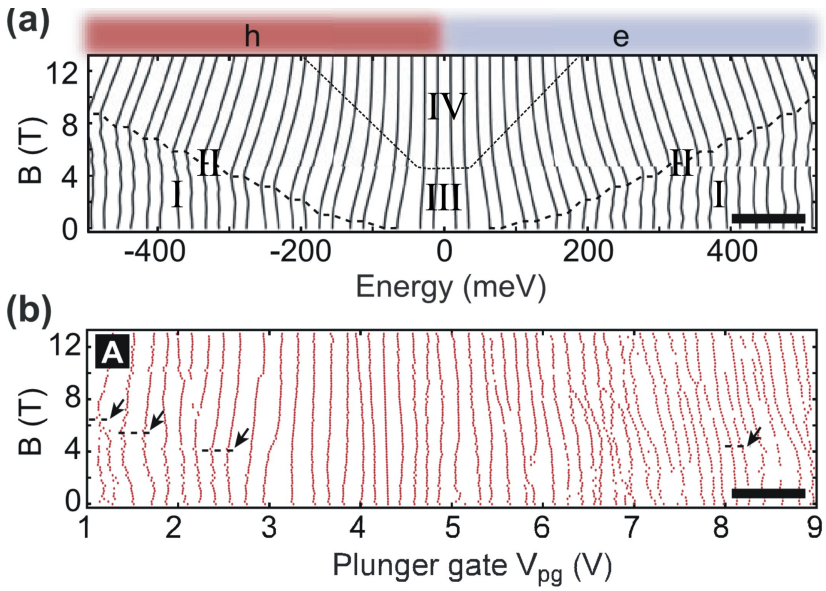

FIG. 4: (a) The Fock-Darwin spectrum of a 50 × 80 nm GQD calculated by assuming a constant charging energy and spin degenerate states. The dashed line (regime II) indicates filling factor ν=2 above which all eigenstates continuously evolve into the zero-energy Landau level. The captions I-IV denote different regimes mentioned in the content. (b) Coulomb peak position as a function of perpendicular magnetic field, measured from the device shown in Fig. 2(a). The arrows indicate the filling factor ν=2 kinks. Adapted with permission from ref. [3]. Copyright 2009 American Physical Society.

Zeeman splitting [the right panel of Fig. 5(c)]. The energy scale of the Zeeman splitting for the spin pairs in Fig. 5(c) and for two additional peak spacings [A3-A4 and A5-A4, not shown in Fig. 5(c)] are plotted in Fig. 5(d). One can see the spin pairs with antiparallel spin (ex: A2-A3, A4-A5) follow the expected Zeeman splitting while the spin pair with parallel spin (A3-A4) has no Zeeman splitting. Apart from the slight deviation of B2-B1, all pairs with antiparallel spin in Fig. 5(d) follow the relation $\Delta E^Z = \pm|g|\mu_B B$ and a g-factor value of approximately 2 can be extracted.

Over the last decade GaAs-based QDs have allowed spin properties to be examined using single spin preparation, manipulation and read-out [7]. Although the 0D states in GQD have shown the ability to store spin, spin-related transport such as Kondo-effect [65] and spin blockade [66] have not been observed in graphene quantum dots so far. This might be attributed to the coupling of spins on the GQD with the magnetic edge states in the GNR tunnel barriers. We will address this issue again in section 2.3 and propose a new type of device to circumvent this problem in chapter 5. In the next section, we will look at charge relaxation dynamics in GQDs.

2.2.3 Charge relaxation measurements

Pulsed gating technique, in which a radio-frequency (RF) voltage is applied to the gates, is a powerful way to manipulate electron spin and to study the spin relaxation time in 2DEG quantum dot systems [7]. When this technique is applied to GQDs, it can be used to investigate excited states (ESs) and relaxation dynamics via pulsed-gate transient current spectroscopy [47, 67]. In these measurements, a rectangular pulse with a duration T [inset in Fig. 6(a)] is applied on top of a DC voltage (V_{PG}) to the plunger gate located in the vicinity of the GQD. If the frequency of the pulse is low ($2/T \leq \Gamma_R$, Γ_L, where $\Gamma_{R(L)}$ is the tunneling rates of the right (left) barrier), the square-wave modulation of the gate voltage results simply in the splitting of the Coulomb resonance into two peaks. Fig. 6(a) shows such a behavior when pulses with increasing amplitude (from bottom to top) are applied to the plunger gate. These peaks [labeled A and B in Fig. 6(a)] result from the QD ground state (GS) entering the bias-window at two different values of V_{PG}, one for the lower pulse-level (A) and one for the upper one (B). The situation changes dramatically at higher frequencies ($2/T \geq \Gamma_R$, Γ_L) as shown in the bottom panel of Fig. 6(b), where the splitting is broadened due to the reduced electron tunneling probability set by T (black dashed line), and a number of additional peaks appear due to transient transport through QD excited states (red dashed line). Each of these additional resonances corresponds to a situation in which the QD levels are pushed well outside the bias-window in the first half of the pulse [Fig. 6(b), top left panel], and then brought into a position where transport can occur only through the ESs in the second one [Fig. 6(b), top middle panel]. While the

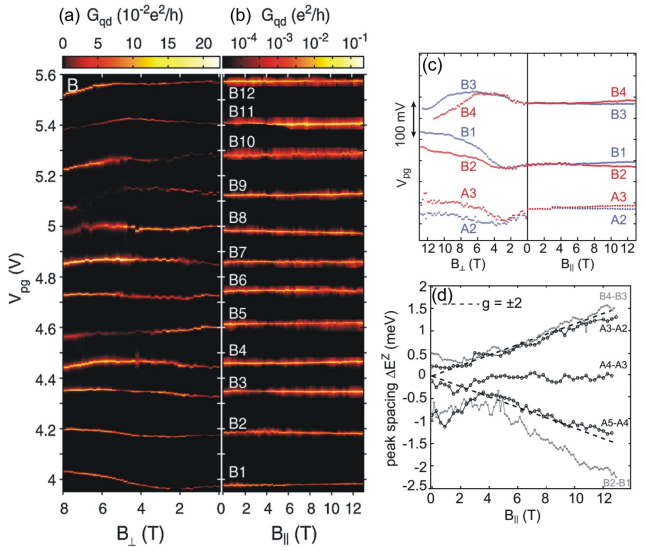

FIG. 5: (a) Coulomb peaks as a function of perpendicular magnetic field recorded at V_b=100 μV, measured from the device shown in Fig. 2(a). (b) The same Coulomb peaks in (a) but measured in parallel (in-plane) magnetic field. (c) Comparing the evolution of three peak pairs in perpendicular (left) and parallel (right) magnetic field. The peak positions are extracted by fitting the data in (a) and (b), and are offset in V_{PG} voltage such that the pairs coincide at B=0 T. (d) Peak spacing as a function of in-plane magnetic field for the three pairs in (c). The dashed lines represent the Zeeman splitting $\Delta E^Z = \pm|g|\mu_B B$ for a g-factor $|g|$=2. Adapted with permission from ref. [49]. Copyright 2010 American Physical Society.

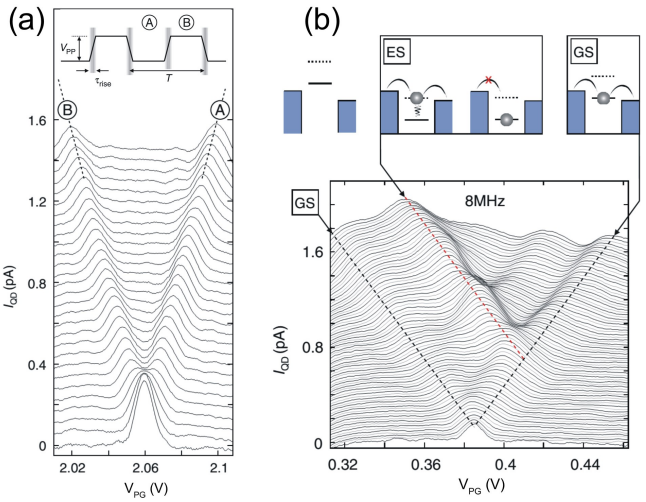

FIG. 6: (a) Current through the dot at V_{SD}=1.5 mV while applying a 100-kHz pulse. Different lines (from bottom to top) correspond to V_{PP} being varied from 0 to 1.4 V in steps of 50 mV. Inset: Sketch of the pulse scheme employed in the measurements presented in this figure. Low and high pulse-level are labeled A and B, and T is the period of the pulse. (b) Top panel: Schematic of transport via GS, ES and, on the left, of a possible initialization stage. Bottom panel: Measurement similar to the ones shown in (a), but with a higher frequency of 8 MHz. V_{PP} is varied from 0 to 2 V in steps of 25 mV (from bottom to top). Adapted with permission from ref. [47]. Copyright 2013 Nature Publishing Group.

ES lie within the bias-window, an electron occupying the GS (either because of tunneling from the leads or relaxation from the ES) will block the current. Therefore, the additional resonances can be resolved in the DC-current measurements only if the frequency of the pulse is higher than the characteristic rate γ of the blocking processes. As both tunneling and ES relaxation lead to the occupation of the GS, γ is approximately given by $\gamma \approx \Gamma + 1/\tau$, where Γ is the tunneling rate from lead to dot and τ is the intrinsic relaxation time of the ES. Since the lowest frequency at which signatures of transport through ESs emerge provides an upper bound for γ while Γ can be determined by the peak current through the dot. This in turn gives a lower bound $\tau \geq 78$ ns for the charge relaxation time of the QD ES. The observed relaxation timescale is related to the lifetime of charge excitations, which is limited by electron-phonon interaction [47]. The fact that it is a factor 5-10 larger than III-V QDs [68–70] perhaps indicates that the electron-phonon interaction in sp^2-bound carbon is weaker due to the absence of piezoelectric phonons.

In this section we have reviewed the transport properties of graphene single quantum dots on SiO_2 in the Coulomb blockaded regime. The Fock-Darwin spectrum in perpendicular magnetic field and the spin states in-plane magnetic field were both studied, as well as the charge relaxation dynamics in GQD's excited states. In the next section, we will review double quantum dots made of graphene.

2.3. Electronic Properties of Graphene Double Quantum Dots

Graphene double quantum dots (GDQDs) are formed when two graphene islands are located close enough such that they are capacitively coupled to each other and separately coupled to adjacent gates. Double quantum dots (DQDs) in a wide range of semiconductors are a model system for investigating the spin dynamics of electrons [7, 71–74]. For example, spin-to-charge conversion using Pauli spin blockade and spin decoherence time measurements, were pioneered in GaAs, and later realized in carbon nanotube and silicon DQDs [7, 8, 66, 75–78]. Graphene has been predicted to be particularly suitable for making spin-based qubits due to the weak spin-orbit interaction and hyper-fine effect [10], which should lead to a long spin relaxation time. However, spin blockade has not been found in GDQD systems so far [50, 51, 79–83]. It has been reported that the spin relaxation time in monolayer graphene ranges from 100 ps to 2 ns, sig-

nificantly shorter than theories predicted [84–88]. Two mechanisms were proposed to explain this observation. One involves local magnetic moments, which enhances spin relaxation due to resonant scattering of electrons off magnetic moments. Nonmagnetic adatoms, organic molecules, vacancies, or spin-active edges are the possible sources [89]. The other is related to the interplay between spin and pseudospin quantum degrees of freedom when disorder does not mix valleys [90]. Due to these mechanisms, electrons spin in GDQDs can be flipped quickly and lift the spin blockade. Despite the failure in manipulating single electron spins in such a system, control of confined charges in GDQD can still be achieved, including gate-tunability of interdot coupling [50, 51, 82, 91] and charge pumping [52], which are introduced in the following sections.

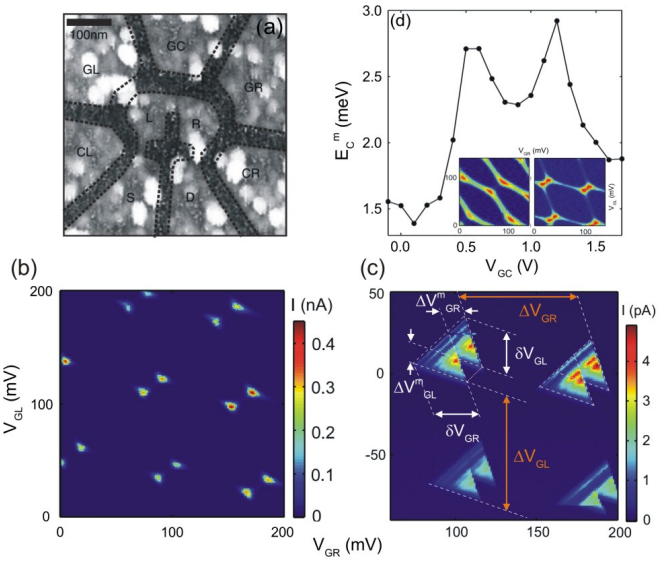

FIG. 7: (a) Atomic Force Microscope image of a graphene double quantum dot (GDQD) etched by O_2 plasma. (b) Current through the double quantum dot as a function of V_{GR} and V_{GL} measured at a low bias voltage V_b=500 μV showing the triple points. (c) The same as (b) but at a higher bias voltage V_b=6 mV shows the bias triangles. (d) Mutual capacitive coupling between the two dots as a function of central plunger gate V_{GC}. All the data points correspond to the same triple point. Inset: Current as a function of V_{GR} and V_{GL} for two different central plunger gate voltages V_{GC}=1.9 V (left) and V_{GC}=0 V (right). Adapted with permission from ref. [80]. Copyright 2010 European Physical Society.

2.3.1 Gate tunable interdot coupling in GDQDs

GDQDs can be fabricated lithographically by O_2 plasma etching out of a graphene flake or by defining the potential landscape using top gates on an etched GNR [50, 51, 79–82]. Fig. 7(a) shows an AFM image of an etched GDQD device on SiO_2/Si substrate. Two plunger gates $V_{GR(GL)}$ are used to tune the energy levels in $QD_{R(L)}$ while three side gates ($V_{CL,GC,CR}$) are used to tune the tunnel barriers. Fig. 7(b) shows the current through the device as a function of V_{GR} and V_{GL} at V_b= 500 μV, in which a honeycomb-like charge stability pattern typical for a double quantum dot device can be seen. In this low bias regime, transmission is only possible within small areas (known as triple points) in the stability diagram where the levels of two dots are aligned with a small bias window. When the applied bias is large, the current flow is possible over a wider range in gate space, resulting in current measured in the bias-dependent triangle-shaped regions (known as bias triangles) as shown in Fig. 7(c). The dimensions of bias triangle allow the determination of the conversion factors between gate voltage and energy. The charging energies for the left dot E_C^L=$\alpha_L \cdot \Delta V_{GL}$=13.2 meV and for the right dot E_C^R=$\alpha_R \cdot \Delta V_{GR}$=13.6 meV are obtained using the voltage-energy conversion factor $\alpha_{L(R)}$=$eV_b/\delta V_{GL(GR)}$ extracted from the bias triangle in Fig. 7(c). The interdot coupling energy can also be determined from the splitting of the triangles [Fig. 7(c)]: E_C^m=$\alpha_L \cdot \Delta V^m_{GL}$=$\alpha_R \cdot \Delta V^m_{GR}$=2.2 meV. It is possible to modulate the interdot coupling strength by changing the voltage applied to the central gate voltage V_{GC}. The inset in Fig. 7(d) shows examples of two charge stability diagrams recorded with exactly the same parameters, except for the voltage applied to the central plunger gate. This is also shown in Fig. 7(d) where the interdot coupling energy E_C^m extracted from the data is plotted as a function of V_{GC}. This oscillating behavior has been reported in three different GDQD devices before and was attributed to resonances induced by disorder states either in the middle GNR (connecting two dots) or in the graphene gate itself [50, 82, 91]. Since large gate-voltage ranges are used, the capacitive coupling of the gates to the disorder states can add or subtract charges discretely to these localized states, thus altering the entire environment abruptly and unpredictably. Consequently, the wavefunction in DQD needs to reconstruct itself, leading to the non-monotonic changes in the inter-dot coupling strength with gate voltage.

2.3.2 Charge pumping in GDQD

Charge pumping, which refers to a device that can shuttle n electrons per cyclic variation of control parameters to give the quantised current $I \equiv nef$, provides an exquisite way to link the electrical current to the elementary charge e and frequency f [92–94]. Such quantized charge transport can be realized when out-of-phase RF signals are applied to the plunger gates of a double quantum dot device [52, 95, 96]. Fig. 8(a) shows a schematic of the measurement circuit and AFM image of a graphene double quantum dot device used for charge

pumping. The AC voltages $V_{RF}(t)$ on both plunger gates with a phase difference φ between them drives the DQD into different charge states around the triple point. When φ= 90, it effectively forms a circular pump loop through three charge states in the stability diagram: (1) loading an electron from source reservoir into the left dot, (2) electron transfer from left dot to the right dot and (3) unloading an electron from the right dot to the drain reservoir, as shown in Fig. 8(a) and (b). When a cycle is complete, a single charge has been transferred from source to drain reservoir and establishes a current. The frequency f of V_{RF} determines the value of the quantized pumped current I=ef while the amplitude of V_{RF} determines the size of area in gate space where pumped current is generated. Depending on the type of triple point that the pumping circle encloses, it generates a different direction of current; i.e. positive current for the electron-transport-type triple point and negative current for the hole-transport-type triple point. Thus, if the pumping is successful the current recorded around two nearby triple points will present a circular shape with equal values but different signs. Fig. 8(c) shows a direct comparison of the locations in gate space around a pair of triple points without RF (top) and with RF (bottom) voltages applied to the plunger gates. If the pump loop only encloses one triple point (green and purple loop), it results in a flat regions, labeled P_+ and P_-, with a quantized pumped current $P_{+,-}$=$\pm ef$ in the stability diagram. However, when the pump loop encloses a pair of triple points (orange loop), it leads to repeatedly increasing and decreasing the occupancy of each QD without any net transfer of electrons from source to drain. Thus, there is a central region (labeled P_0) where $I\approx$0, giving rise to the crescent shape of pumped current as shown in Fig. 8(c). Unambiguous confirmation of quantized charge pumping is shown in Fig. 8(d), which plots the pumped current as a function of f with the DC gate voltages fixed at the center of the P_+ region. The oscillatory behavior is introduced because of a frequency-dependent phase shift in the RF circuit. The pumped current follows the quantized value I=$\pm ef$ over a range of frequencies up to gigahertz, an order of magnitude faster than the traditional metallic pump [97]. The pumping frequency in graphene is characterized by the RC time constant of the tunnel barrier, where R and C are the effective resistance and capacitance of the GNRs. The two-dimensional nature of graphene leads to a small C and results in a large pump frequency set by the tunnel rate of tunnel barriers (GNRs) [52].

Up to now, we have reviewed the transport properties of GQDs which are fabricated by E-beam lithography and O_2 plasma etching. In the next section, we review another type of quantum dot that is defined from the deformation of graphene membrane.

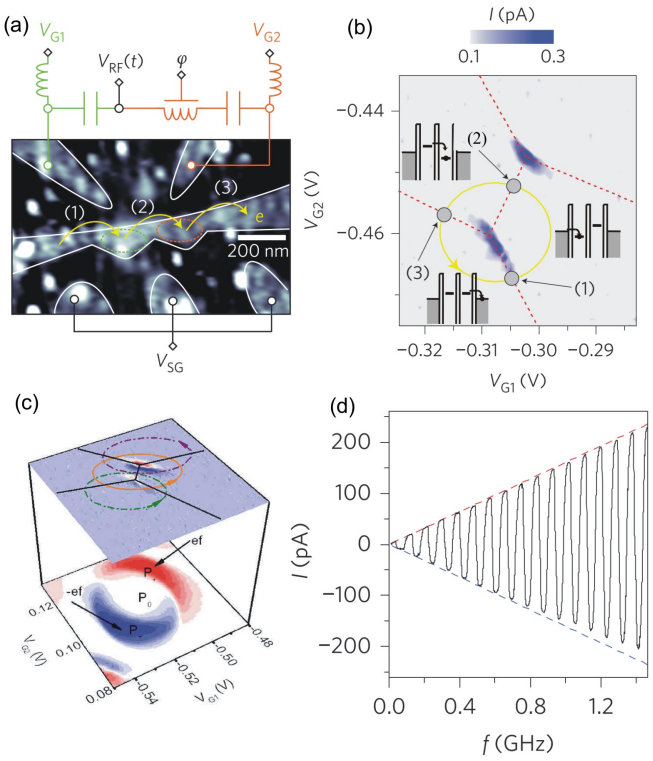

FIG. 8: (a) Atomic force micrograph of the device that shows the gates used to generate the pumped current in a GDQD device. An oscillating voltage $V_{RF}(t)$ is added to the DC voltages V_{G1} and V_{G2}. A phase difference φ is added to V_{RF} before being added to one of the gates, which describes a circular trajectory (yellow circle) shown in (b). (b) Source-drain current as a function of V_{G1} and V_{G2} with an applied bias $\leq$1 μV. The trajectory (yellow) that encircles a triple point, passing through the sequence of transitions (1)→(2)→(3) as indicated in both (a) and (b). The insets denote different configuration of QD's energy level. (c) Plot showing a direct comparison between the DC (top) and AC (bottom) current behavior with f =12 MHz and P =-25 dBm. Regions P_+, P_- and P_0 refer to the positive, negative and zero pumped current, respectively. (d) Pumped current as a function of frequency at a power of P=-15 dBm. Adapted with permission from ref. [52]. Copyright 2013 Nature Publishing Group.

2.4. Strain induced quantum confinement in graphene

When graphene is deformed, the strain in the membrane can induce a local pseudomagnetic field, which has been reported to be as high as a real magnetic field of 300 T [98–100]. This strain-generated pseudomagnetic fields can introduce strong quantum confinement to electrons, from which a quantum dot can be formed [57]. Fig. 9(a) shows a scanning tunneling spectroscopy (STS) setup used to study the electronic properties of such a QD. The suspended graphene, as shown in Fig. 9(b), is fabricated by exfoliation of graphite onto the prepatterned SiO_2/Si substrate. Both the van der Waals forces

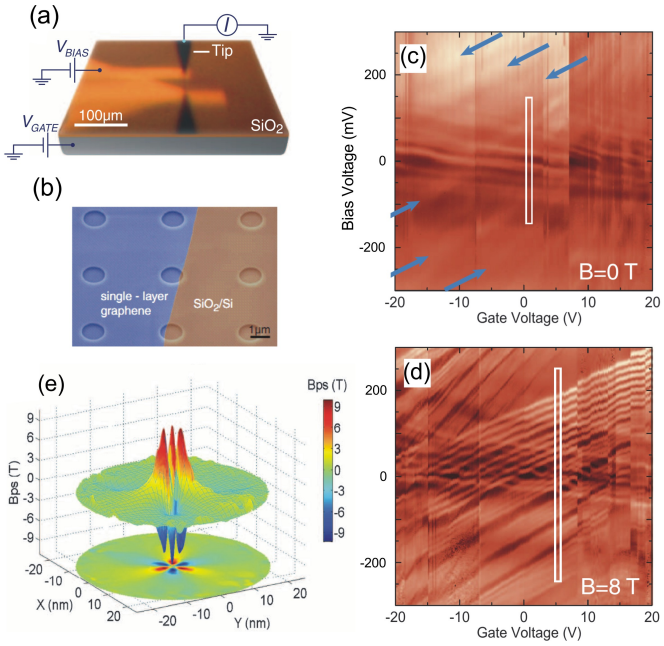

FIG. 9: (a) Scanning tunneling spectroscopy (STS) setup. (b) Scanning electron microscope image of the suspended graphene device. (c) dI/dV gate-map spectra on the suspended graphene membrane at B=0 T. (d) Same as (c) but at B=8 T. (e) The pseudomagnetic field, calculated based on the strain field in (d), shows a spatially alternating field with threefold symmetry that can spatially confine carriers. Adapted with permission from ref. [57]. Copyright 2012 American Association for the Advancement of Science.

from the STS tip and electrostatic force induced by back-gate voltage can induce mechanical deformation in the suspended graphene membranes, and the tunneling current between the tip and graphene is measured simultaneously. The evidence for 0D behavior can be seen in Fig. 9(c) and (d), where dI/dV spectra (I is the tunneling current) at different B-fields are measured as a function of both tunneling bias (V_{BIAS}) and back-gate voltage (V_{GATE}), with the tip position fixed at the center of the graphene membrane. In contrast to the data measured at B=0 T, a series of resonances with equal spacing appear as tilted lines in the map at B=8 T, indicating electrical tunneling to the QD energy levels and the simultaneous gating effect from the back-gate voltage and tip bias. In order to provide deeper insight into the observed 0D behavior at B=8 T, Fig. 9(e) shows the calculated pseudomagnetic field in the suspended membrane. The pseudomagnetic field (alternating between ±10 T) spatially confines the carriers in graphene, forming clockwise and counterclockwise orbits around the alternating peaks of the pseudomagnetic field. However, at some areas where the pseudomagnetic field changes sign, the pseudofield is not strong enough to confine electrons. The overall confinement can be improved if an external magnetic field is applied to block those leaky paths, resulting in a well defined QD energy spectrum as seen in Fig. 9(d). The charging energy extracted from the level spacing in the gate map [see rectangle in Fig. 9(d)] varies from 11.7 to 5.3 meV. Using the capacitance model this corresponds to a dot size ≈34 to 53 nm in diameter [57], in reasonable agreement with the size of the estimated pseudomagnetic field [45 nm, Fig. 9(e)], reinforcing the idea that dot is formed using strain engineering in graphene.

In chapter 2, we have reviewed the transport properties of graphene single dots and double dots fabricated on SiO_2 substrate. We summarized the main observations with references in Table I. In the next chapter, we review graphene nanostructures fabricated on hexagonal boron nitride (hBN) to reduce the influence of substrate disorder.

TABLE I. Reference with the main observations

References	Main observations in graphene single quantum dots (GSQDs)
[1]	Observation of excited states
[2]	Charge detection
[3, 48]	Fock-Darwin spectrum in the few electron and many electron regime
[49]	Zeeman splitting of spin states
[54]	First suspended GQD
[53, 54, 101]	Bilayer GQD defined by top gate
[47, 67]	High-frequency gate manipulation on GQD
[57]	GQD defined by stain engineering
References	Main observations in graphene double quantum dots (GDQDs)
[50, 51, 80]	Observation of excited states
[51]	Zeeman splitting
[51, 102]	Bilayer graphene double dot
[50]	GDQD defined by gated-GNR
[103]	Electron-phonon coupling
[82]	Metal gate tuning
[52]	Charge pumping
[104]	Charge redistribution

3. GRAPHENE NANOSTRUCTURES ON HBN

Hexagonal boron nitride (hBN) is isostructural to graphene but has boron and nitrogen atoms on the A and B sublattices, leading to an insulator with a large band gap of around 6 eV [11, 13, 105–107]. The planar nature and the ionic bonding of hBN enable it to be cleaved into an ultra-flat sheet free of dangling bonds, pinholes and charge traps at the surface [108]. Indeed, the use of hBN thin films as a dielectric layer for gating or as a flat substrate for graphene transistors has shown

to improve the electronic transport quality of devices by a factor of ten or more compared to the case of graphene on SiO_2 substrates [12, 14–16]. For example, Amet *et al.* reported a graphene-on-hBN device exhibiting a mobility as high as 10^6 $cm^2V^{-1}s^{-1}$, as well as narrow Dirac peak resistance widths, indicating reduced disorder and charge inhomogeneity [109]. In order to make clean interface between graphene and hBN, a polymer-free dry transfer technique is commonly adopted [12, 110–112]. Fig. 10(a) shows a hBN/graphene/hBN stacking made from such a dry transfer, in which a pre-exfoliated hBN on poly-propylene carbonate (PPC) is used as a stamp to pick up alternating layers of graphene and BN, as illustrated in Fig. 10(b). hBN has an atomic-level smooth surface that can suppress surface ripples in graphene. STM topographic images [Fig. 10(c)] show that roughness of graphene on hBN is greatly decreased compared to that of graphene on SiO_2 substrates. While graphene on SiO_2 exhibits charge puddles with diameters of 10∼30 nanometers, the size of charge puddles in graphene on hBN are roughly one order of magnitude larger.

Due to the similarity in lattice structure, when graphene is stacked on hBN with a small twist angle ($\leq 5^\circ$) it can form a superlattice [moire pattern, as shown in Fig. 10(d)] with a wavelength ranging from a few to 14 nm [14–16, 113]. The moire pattern of graphene/hBN stacks can introduce minibands and a small gap around the K points in graphene's band structure [16]. Fig. 10(e) shows typical transfer curves for three graphene/hBN stacking with different moire wavelengths, in which two extra Dirac peaks, situated symmetrically about the charge neutrality point (V_g=0 V), are observed in all devices. These newly appeared Dirac peaks result from superlattice minibands away from the original Dirac point of graphene, as shown in the inset of Fig. 10(e). Such hybrid band structures lend novel transport features to graphene, for example, the discovery of Hofstadter Butterfly spectrum in high magnetic fields [14–16].

While the behavior of graphene nanostructures fabricated on SiO_2 is clearly influenced by localized states, it remains an open question whether they originate predominantly from substrate disorder or edge roughness. In the following, we review the studies of graphene nanodevices fabricated on hBN substrate. These devices, with reduced substrate disorder potential, are expected to enable the influence of substrate and edge disorder to be studied separately.

3.1. GNRs on hBN

Graphene constrictions fabricated on hBN substrate with micrometer and a few tens of nanometer scales have been investigated so far [114, 115]. While the micron-sized graphene constrictions on hBN indeed showed an improved mobility (55000 $cm^2V^{-1}s^{-1}$) and reduced disorder density (below 10^{10} cm^{-2}), no major differences were observed for the graphene nanoribbons, as shown in the right panel of Fig. 11(a), compared to their counterparts on silicon dioxide [114]. In both cases, electrical transport is characterized by the percolation process through localized charge puddles formed along the GNRs. It leads to a conclusion that the edges - which are expected to be similar for reactive-ion-etched ribbons on both SiO_2 and hBN - dominate charge transport in those long graphene nanostructures (W=80 nm, L=240 nm). However, a new feature emerged when a relatively short GNR (30 nm × 30 nm), as shown in the left panel of Fig. 11(a), was studied on hBN substrate [115]. Fig. 11(b) shows the differential conductance as a function of applied DC bias and back-gate voltage for this device. A series of Coulomb diamonds are present in the transport gap, showing the existence of localized states in the GNR. Fig. 11(c) shows a close-up of a region highlighted by orange rectangle in Fig. 11(b). The smallest observed diamonds [dotted line in Fig. 11(c)] spanning about 0.1-0.2 V in back-gate voltage corresponds to a capacitance of 1.6-0.8 aF ($C_{BG,loc} = e/\Delta V_{BG}$). Employing the plate capacitor model corrected with a factor of 1.5 for stray fields, the area of a site of localized charge can be calculated using $A \approx \frac{ed}{\epsilon\epsilon_0 \Delta V_{BG}} \times \frac{1}{1.5}$, where ϵ and d are the dielectric constant and thickness of SiO_2 [115]. Surprisingly, the area associated with a diamond spanning 0.1 V in back-gate, for example, is estimated to be 9000 nm^2 and is ten times larger than the geometrical constriction size ($(30\ nm)^2$). To address this observation, a tight-binding simulation was performed to calculate the wave function in a 30×30 nm GNR connected to 140 nm wide graphene leads, as shown in Fig. 11(d). Note that the random fluctuations of the boundary with an amplitude of 2 nm is introduced to address the edge roughness. As can be seen, states localized mostly in the constriction (middle panel) will contribute to the Coulomb blockade and are likely to result in wide diamonds. On the contrary, some states are strongly localized at an edge outside of the constriction (left panel) which do not contribute to the transport. However, there are a number of strongly localized states, as shown in the right panel of Fig. 11(d), that localize along the rough edge of the constriction and extend along the edge also into the leads of the device. These states are potentially responsible for the smaller diamonds observed experimentally [Fig. 11(c)]. While the consideration of graphene leads is the key factor for the extension of wavefunction, two conditions are also crucial for this effect to be seen. One is that the substrate disorder has to be much weaker than the edge disorder, and the other is the edge-to-bulk ratio of device has to be large enough for the edge to play an important role. In the next section, a transport work on GQD on hBN will show that the substrate is the dominant source of disorder for QD size larger than 100 nm in

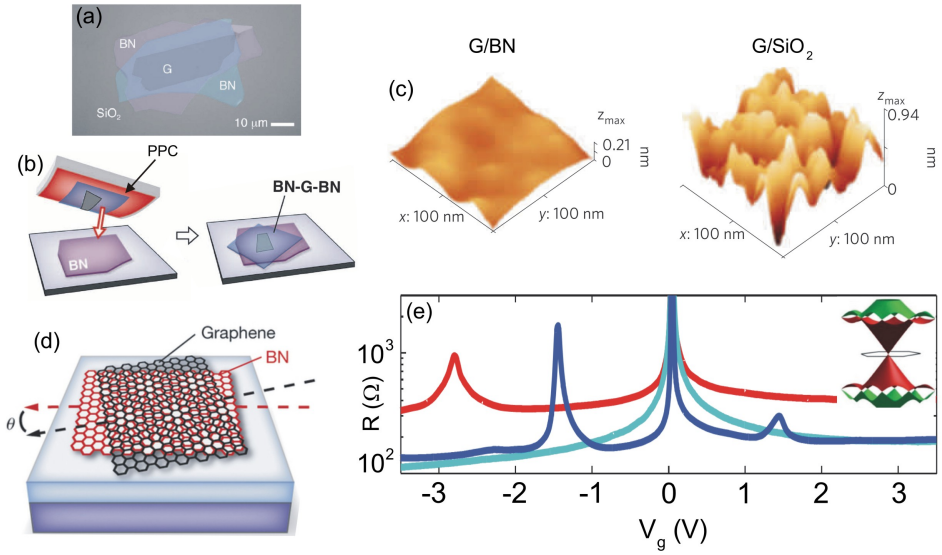

FIG. 10: (a) Optical image of a multilayered heterostructure fabricated using the process illustrated in (b). (b) Schematic of the dry-transfer technique for stacking layered materials. (c) STM topographic images of monolayer graphene on hBN (left) and SiO_2(right) showing the underlying surface corrugations. (d) Schematic of the Moire pattern formed from a graphene/hBN stack. The Moire wavelength varies with the twist angle θ. (e) Resistance as a function of gate voltage measured from three G/hBN devices (with different moire wavelengths), showing two extra Dirac peaks as a result of the superlattice minibands. Inset shows the band diagram of graphene on hBN. (a, b) adapted with permission from ref. [112]. Copyright 2013 American Association for the Advancement of Science. (c) adapted with permission from ref. [108]. Copyright 2011 Nature Publishing Group. (d) adapted with permission from ref. [14]. Copyright 2013 Nature Publishing Group. (e) adapted with permission from ref. [16]. Copyright 2013 American Association for the Advancement of Science.

diameter. Therefore, for wider GNRs (smaller edge-to-bulk ratio) or GNRs on SiO_2 (strong substrate disorder), localization along the edge still happens but bulk contributions are expected to dominate transport.

3.2. GQDs on hBN

Graphene quantum dots with different diameters ranging from 100 to 300 nm have been fabricated on hBN substrate for electrical investigation [116, 117]. The sizes of the dots are close to the order of the expected size of charge puddles in bulk graphene on hBN [108]. Fig. 12(a) shows the schematic illustration of such a device (top panel) and atomic force micrograph of an etched graphene QD on hBN with a diameter of 180 nm (bottom panel). The QD levels are tuned by a plunger gate (PG) while two side gate (SGR and SGL) are used to tune the resistance of the tunnel barrier GNRs. In a regime where the two barriers are pinched-off, the current I_{SD} as a function of plunger gate voltage, as shown in Fig. 12(b), confirms that the QD is in the Coulomb blockade regime. For a more detailed comparison between QDs resting on hBN and SiO_2, the distribution of the Coulomb-peak spacing ΔV_{PG}, i.e., the spacing between two subsequent Coulomb peaks, are statistically studied among different dots fabricated both on hBN and SiO_2 substrate. The normalized Coulomb peak spacings $\Delta V_{PG}/\overline{\Delta V_{PG}}$ for QDs on hBN are reported as histograms in Fig. 12(c), for QD diameter d=110 nm (left panel), d=180 nm (middle panel) and d=300 nm (right panel) respectively. The same type of measurements are also performed for QDs on SiO_2, and the results are summarized in Fig. 12(d), where the standard deviation of the normalized peak spacing distribution (σ) as a function of the QD diameter is presented for both hBN and SiO_2 substrate. A clear difference can be seen between these two cases. The standard deviation for QD on hBN shows a clear decreasing dependence from 0.16 for the dot with d=110 nm to 0.05 for the dot with d=300 nm, while in the case of QD on SiO_2 it is independent of d. The standard deviation σ, which can be considered as the strength of peak-spacing fluctuations, may result from (i) the fluctuations of single particle level spacing Δ, (ii) fluctuations of the charging energy E_C (i.e., fluctuations in the size of the dot), or (iii) fluctuations of the lever arm α (i.e., the position of the dot). The single particle level spacing in GQD is $\Delta(N)=\hbar v_F/(d\sqrt{N})$, where N is the number of charge carriers on the dot and v_F is the Fermi velocity [1]. If N is the only variable, the single particle level spacing $\Delta(N)$ gives an upper limit at the order of 0.03 to σ for N= 600 (the number of peaks studied), and should be independent of the dot size and substrate. This is not in agreement with the data shown in Fig. 12(d) and leads to the assumption that the main source of variability in peaks spacing re-

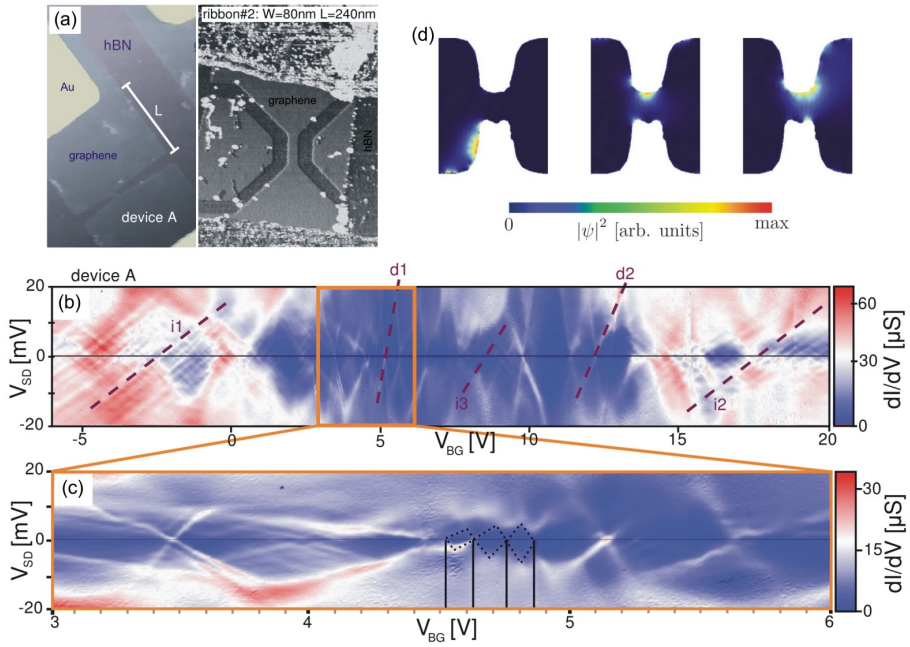

FIG. 11: (a) Scanning force microscopy images of two GNR/hBN devices with different geometries. (b) Differential conductance of device A [left panel in (a)] as a function of applied back-gate and bias voltage. (c) Closeup of a region highlighted by yellow rectangle in (b). (d) Results for the tight-binding simulation of a 30×30 nm GNR connected to open leads of width 140 nm. ψ in the color bar denotes the wavefunction. Each panel corresponds to an eigenstate which is localized in different area of device. Adapted with permission from ref. [115]. Copyright 2014 American Physical Society.

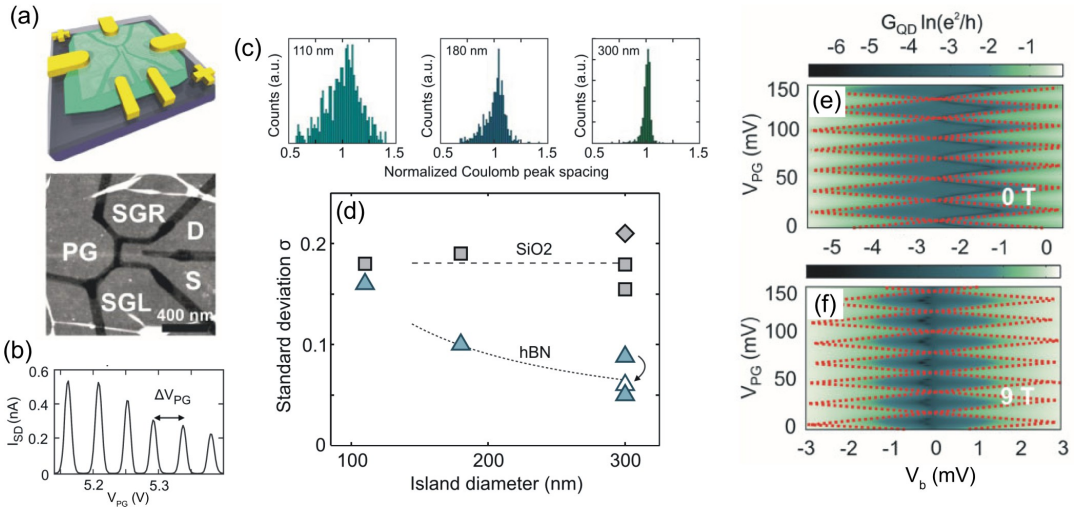

FIG. 12: (a) Top panel: Schematic illustration of a graphene SET on hBN. Bottom panel: Atomic force micrograph of an etched GQD on hBN with a diameter of 180 nm. (b) Source-drain current I_{SD} as a function of V_{PG} for the device shown in (a). (c) Normalized peak-spacing distribution for GQDs on hBN with diameters of d=110 nm (left panel), d=180 nm (middle panel), and d=300 nm (right panel). (d) Summary plot of the standard deviation σ of the normalized peak-spacing distribution for different sized GQD on a SiO_2 (rectangular data points) and hBN (triangular data points) substrate. (e) Coulomb Diamond measurement of a GQD (d=300 nm) on hBN at a perpendicular B-field of 0 T. (f) The same measurement as (e) but at B=9 T. (a, b, c, d) adapted with permission from ref. [116]. Copyright 2013 American Institute of Physics. (e, f) adapted with permission from ref. [117]. Copyright 2013 John Wiley and Sons.

sults from the change in the dot diameter d and the lever arm α. The standard deviation for GQD on hBN can be represented as $\sigma \approx \sigma^{hBN} + \sigma^{edge}/d \approx 0.01 + 16/d$ [nm], where σ^{hBN} represents the substrate-induced disorder (independent of dot size) and σ^{edge} represents the edge-induced disorder (scale with size as the edge-to-bulk

ratio changes). Note that both values are obtained from the fit of the dotted line in Fig. 12(d). On the contrary, the standard deviation for QD on SiO_2 is independent of dot size and reads $\sigma^{SiO_2} \approx 0.18$. This suggests that the potential landscape in the dot on SiO_2 is dominated by substrate induced disorder, while contributions due to edge roughness, which are expected to scale with the size of the sample, play a minor role. These values lead to the conclusion that (i) the substrate induced disorder in graphene QDs on hBN is reduced by roughly a factor 10 as compared to SiO_2 (σ^{SiO_2}=0.18 to σ^{hBN}=0.01), (ii) edge roughness is the dominating source of disorder for QDs with diameters less than 100 nm.

The reduced substrate disorder of GQD on hBN can also reflect on the magneto-transport. If the magnetic length of the electrons on the graphene QD is on the order of the disorder potential length scale, the electrons can accumulate in different charge puddles, leading to breaking apart the dot thus changing the charging energy. However, as a result of the reduced bulk disorder, the breaking apart for GQD on a hBN substrate is assumed not to occur. Fig. 12(e)(f) show the comparison of Coulomb diamond measurements of a d=300 nm GQD on hBN at B=0 T and B=9 T. It can be seen by the Coulomb diamond with a charging energy $E_C \approx 3$ meV for both magnetic fields, that the QD is stable and well-defined at 9 T, supporting the notion that the GQD is not breaking apart in high magnetic fields.

In summary, we have reviewed the transport properties of GNRs and single GQDs on hBN substrate. The effect of reduced substrate disorder can be observed both in GNRs (smaller Coulomb diamond) and GQDs (Coulomb peak spacing fluctuating with QD's size). However, although not being reported so far, the spin related transport such as spin blockade are still expected to be altered by the edge state in the etched GNR tunnel barriers. Further work is needed to replace the GNR with magnetic inert tunnel barriers (such as hBN) to reduce the edge effect and revisit the spin related physics in GQDs. In the next chapter, we will review nanostructures made of topological insulators, whose surface state is graphene-like but with its own spin-texture and is promising for realizing room-temperature spin qubit devices.

4. NANOSTRUCTURES OF TOPOLOGICAL INSULATOR

Topological insulators (TIs) are materials with a large band gap like ordinary insulators but have a gapless Dirac states on the edge or surface [22]. Such surface states are metallic and robust against disorder, as long as no magnetic fields or magnetic impurities break time-reversal symmetry. The first demonstrated TI is a quantum well structure where HgTe thin film is sandwiched between two layers of CdTe [118]. The opposite parity of p level and s level in HgTe compared to those in CdTe leads to a band crossing in HgTe, from which the edge states can be formed. The resulting 2D TI and the corresponding edge state dispersion are illustrated in Fig. 13(a). It can be seen from the edge dispersion that the electron with reversed wavevector has opposite spin polarization, so the spin-up and spin-down electrons counter-propagate along the edge. Such edge state resembles the Quantum Hall edge state, in which dissipationless current flows along the sample edge, except the edge current is now spin-polarized and no magnetic field needs to be applied to the sample. 3D topological insulators, such as $Bi_{1-x}Sb_x$ and Bi_2Se_3, were predicted and recently identified experimentally [119–124]. Compared to 2D TIs, the edge states now form metallic surfaces state covering the entire material as shown in Fig. 13(b). Its band structure [right panel of Fig. 13(b)] shows that electron with positive surface wavevector k has opposite spin orientation to the electron with negative surface wavevector -k, which is generally referred as spin-momentum locking in TIs. The surface state in 3D TI can be viewed as Dirac fermion in graphene but without the two-fold valley and spin degeneracies, and is topologically protected from backscattering by time-reversal symmetry.

Topological surface states are ideal for certain applications in low-power electronics [127] and quantum computing devices [128, 129]. However, electron-transport measurements on the TI surface states sometimes involve the unavoidable residual bulk carriers. TI nanostructures offer several advantages to overcome this problem and enable studying the fundamental nature of the topological surface states. First, their large surface-to-volume ratio greatly reduces the bulk carrier contribution in the overall electron transport. Second, TI nanostructures have well-defined nanoscale morphology, ideal for quantum interference experiments such as Aharonov-Bohm (AB) oscillations. Third, the field-effect gating to tune the Fermi level in TI nanostructures is relatively easy, due to the fact that they are only tens of nanometers thick. Thus, the design of nanostructures on TI is attractive both in probing the nature of confined topological modes [130, 131] as well as the possibility of using them as building block for quantum information applications [132, 133].

Bi_2Se_3 is a 3D topological insulator, in which Se-Bi-Se-Bi-Se are bonded covalently into a quintuple layer (QL), and a crystal is formed *via* van der Waals force connecting each QL as shown in Fig. 13(c). Unlike $Bi_{1-x}Sb_x$ alloy, Bi_2Se_3 is stoichiometric compound which can be mechanically exfoliated from bulk at higher purity [see Fig. 13(d)] [129, 134]. In addition, the large enough bulk band gap (0.3 eV) equivalent to 3,600 K enables the topological phase to be seen at room temperature [123]. Fig. 13(e) shows an angle-resolved photoemission spectroscopy (ARPES) measurement on Bi_2Se_3, where only a single surface state with electronic dispersion almost the

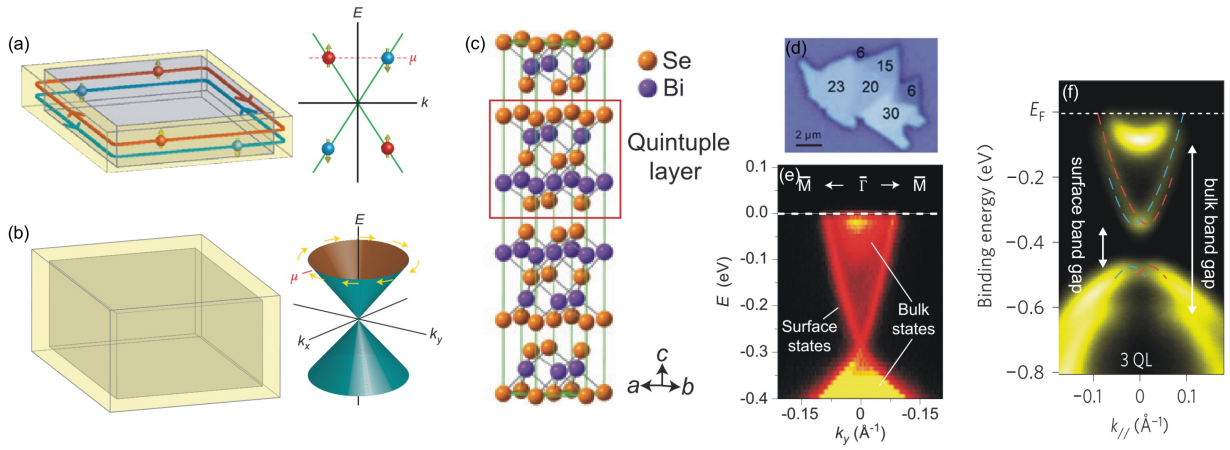

FIG. 13: (a) (Left): Schematic illustration of the metallic edge (shown in yellow) of a 2D topological insulator, in which spin-up and spin-down electrons counter-propagate. (Right): The corresponding idealized spin-resolved band structure of the edge states. μ denotes the Fermi level. (b) (Left): Schematic illustration of the metallic surfaces (shown in yellow) of a 3D topological insulator. (Right): The corresponding idealized band structure of the surface states, revealing chiral lefthanded spin-texture which is sometimes referred as spin-momentum locking. (c) Layered crystal structure of 3D topological insulators Bi_2Se_3. Each layer consists of five atomic sheets (a quintuple layer, QL) and each QL is bonded together by van der Waals interactions along the c-axis. (d) Optical micrograph of Bi_2Se_3 thin flakes produced by mechanical exfoliation. The overlaid numbers indicate the number of QLs. (e) Angle-resolved photoemission spectroscopy (ARPES) measurements of surface electronic band dispersion on Bi_2Se_3 along the $\overline{\Gamma}$-$\overline{M}$ momentum-space cut. (f) ARPES spectrum (along the $\overline{\Gamma}$-$\overline{K}$ direction) of a three QL Bi_2Se_3 slab shows a gap opening in the surface states. (a, b, c, e) adapted with permission from ref. [20]. Copyright 2011 Nature Publishing Group. (d) adapted with permission from ref. [125]. Copyright 2011 American Physical Society. (f) adapted with permission from ref. [126]. Copyright 2010 Nature Publishing Group.

same as an idealized Dirac cone is present. In order to induce quantum confinement in Bi_2Se_3, a band-gap has to be introduced in the gapless surface states. This can be achieved by thinning Bi_2Se_3 into a thin slab. The tunnel coupling between the top and bottom surface induces a symmetry-breaking and creates a thickness-dependent surface band gap [126, 135] as exampled in Fig. 13(f). The other approach is to place magnetic materials proximity to a TI, in this way the broken time-reversal symmetry can result in a surface band gap at the interface [136–139]. In the following sections, we will focus on Bi_2Se_3 nanostructures (including nanowires and quantum dots), in which synthesis methods and their transport properties will be reviewed.

4.1. Bi_2Se_3 nanowires

Methods for producing topological insulator nanomaterials can generally be categorized as bottom-up synthesis and top-down exfoliation [20]. The top-down exfoliation is the so-called scotch tape method, which is commonly used to exfoliate graphene from natural graphite. As for the bottom-up approach, topological insulator nanoribbons are made by Au-catalyzed vapor-liquid-solid (VLS) growth in a tube furnace [140, 141]. In such a growth, the source material Bi_2Se_3 powder is placed in the hot center of the furnace while Si substrates coated with 20 nm Au nanoparticles are placed in the downstream side of the furnace. The furnace is then heated to high temperature in the range of 450-580 °C and is kept at the high temperature for 1-5 h, followed by a natural cool-down period. The SEM images of the as-grown Bi_2Se_3 nanowires and nanoribbons are shown in Fig. 14(a) and (b), respectively. At the warm zone of the furnace, the growth of quasi-one-dimensional materials is dominant [see Fig. 14(c), (d), (e)] while at the cool zone the nanoribbons with lateral dimensions of several micrometers are the dominant growth product [see Fig. 14(f)]. The use of Au nanoparticle as catalyst induces the nucleation and growth of the nanomaterial, their presence at the end of each nanowire and nanoribbon can be viewed as an evidence of VLS growth mechanism. The thickness of these ribbons is roughly determined by the size of the Au nanoparticles (few nanometers), and the width of the ribbon varies from 50 nm to tens of micrometers. Another approach to fabricate thin Bi_2Se_3 nanoribbons down to few nanometers is shown in Fig. 14(g), where an atomic force microscope tip is used to sweep off the extra layers of Bi_2Se_3 to form a thinner ribbon [142].

TI nanowire is ideal for studying the quantum interferences of the topological surface states due to its well-defined nanoscale morphology. Aharonov-Bohm (AB) oscillations are particularly suitable to probe the surface states since a quantum phase is introduced when surface

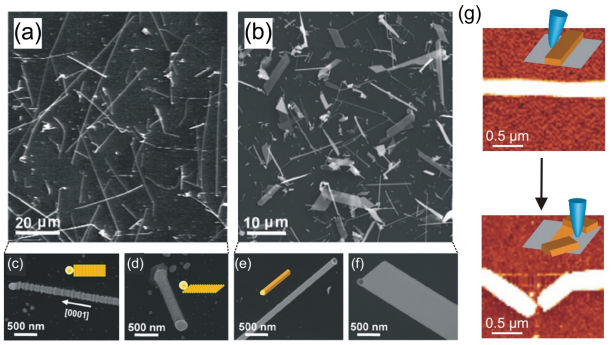

FIG. 14: Scanning electron microscope (SEM) images of Bi_2Se_3 nanostructures grown via VLS method. (a) SEM image of Bi_2Se_3 nanowires grown on a warm substrate. (b) SEM image of Bi_2Se_3 nanoribbons grown on a cool substrate. (c) Nanowire grown along c-axis. (d) Nanowire grown off c-axis. (e) Quasi-1D narrow nanoribbon. (f) Sheetlike wide nanoribbon. (g) Exfoliation of Bi_2Se_3 nanoribbons using an AFM, in which multiple layers of the materials are knocked off by the tip. (a, b, c, d, e, f) adapted with permission from ref. [140]. (g) adapted with permission from ref. [142]. Copyright 2010 American Chemical Society.

electrons complete a close loop along the perimeter of TI nanowire. However, the AB oscillations in TI nanowires in fact suggest a different type of B-filed modulation on its electronic band structure as can be seen below. When the surface electrons mean free path exceeds the perimeter of the TI nanowire, the conical band dispersion of 2D Dirac Fermions transform into discrete 1D subbands due to the quantum confined periodic boundary condition along the perimeter direction. This mimics the transition from graphene to a carbon nanotube, except for the fact that TI surface states are spintextured as shown in Fig. 15(a). Interestingly, these 1D subbands can be periodically modulated by a magnetic flux Φ, described by $E(n,k,\Phi) = \pm h v_F \left[k^2/4\pi^2 + (n + 1/2 - \Phi/\Phi_0)^2/L^2\right]^{1/2}$, where n is the subband index (integer), Φ_0=h/e, and h and v_F are the Plank constant and Fermi velocity, respectively. This 1D band dispersion gives rise to a h/e periodicity in magnetoconductance oscillations and is in contrast to the $h/2e$ period oscillations in metallic cylinder conductors (known as Altshuler-Aronov-Spivak (AAS) oscillations). Such B-field dependency comes from the spin-momentum locking property of the TI surface electrons, which adds a Berrys phase (π) to the electron wave function when spins of the surface electrons make a 2π rotation along the nanowire circumference. Thus, all the 1D subbands of surface electrons are gapped at zero magnetic field [Fig. 15(a)] but can be restored to a gapless 1D mode when the magnetic flux $\Phi = \pm h/2e$ (for n = 0), $\pm 3h/2e$ (for n = 1).., as shown in Fig. 15(b).

Fig. 15(c) shows a false-colored scanning electron microscope image of heterostructure nanowire that is used to study the AB magnetocondcutance oscillations. It consists of a Bi_2Se_3 core (40 nm height × 120 nm width) and an amorphous Se shell (2 nm), which are synthesized using the VLS growth as discussed before. A magnetic field is applied along the nanowire length to introduce magnetic flux encircled by electrons moving along perimeter of the nanowire. The AB interference measurements at different applied back-gate voltages are shown in the right panel of Fig. 15(d), while the associated Fermi energy is indicated in the left panel. Two period oscillations at $h/2e$ and h/e are observed, in which $h/2e$ period is from AAS effect (peaks at $\Phi = 0, \pm h/2e, \pm h/e..$) and h/e period is from periodic modulation of 1D subband by magnetic flux (peaks at $\Phi = \pm h/2e, \pm 3h/2e..$). Note that the AAS peaks at $\Phi = \pm h/2e, \pm 3h/2e..$, etc are relatively weak compared to these at $\Phi = 0, \pm h/e..$, etc [see topright panel of Fig. 15(d)]. The evidence for the quantum oscillations from 1D subband model is the electrical gate modulation. When the Fermi energy is far away from the Dirac point [highlighted by blue rectangle in Fig. 15(d)], the Fermi level crosses multiple 1D subbands. The change of DOS induced by the magnetic flux (one subband's DOS) is much smaller than the total DOS (entire subbands' DOS), resulting in small oscillation amplitude at $\Phi = \pm h/2e, \pm 3h/2e..$, *etc.* The oscillation amplitude at half quantum flux can be enhanced when the Fermi energy is tuned closer to the Dirac point [highlighted by red rectangle in Fig. 15(d)], where the Fermi level crosses less 1D subbands and the change in DOS induced by the magnetic flux becomes pronounced at $\Phi = \pm h/2e, \pm 3h/2e..$, etc. This gating effect on the magnetoconductance oscillations is even stronger in a thinner nanowire (10 nm height × 50 nm width), where the 1D band gap is now large and enable to reach the Dirac point by gating. The magnetoconductance oscillations of this device at two different back-gate voltages are shown in the right panel of Fig. 15(e), with the the associated Fermi level shown in the left panel. As can be seen, when the Fermi level is at the Dirac point (red dashed line and red rectangle), there exists no 1D electronic state at zero magnetic field, resulting in no peak at $\Phi = 0$. However, when the additional magnetic flux restores the gapped 1D band to the gapless 1D state, the oscillation peak is found at $\Phi = \pm h/2e$. The different nature of gapped 1D mode ($\Phi = 0$) and gapless 1D mode ($\Phi = \pm h/2e$) can be clearly demonstrated by gate voltage sweep as shown in Fig. 15(f). In the case of zero magnetic flux ($\Phi = 0$), the resistance starts to diverge near the Dirac point (V_G= -22 V) due to the gapped 1D subband. On the contrary, in the case of $\Phi = \pm h/2e$ resistance converges around the Dirac point, indicating the Fermi level is tuned across the gapless (helical) 1D state. A more detailed study of the gapless state at $\Phi = \pm h/2e$ revealed that it is robust against additional impurities but can be easily destroyed under time-reversal symmetry breaking (i.e., perpendicular magnetic field) [5].

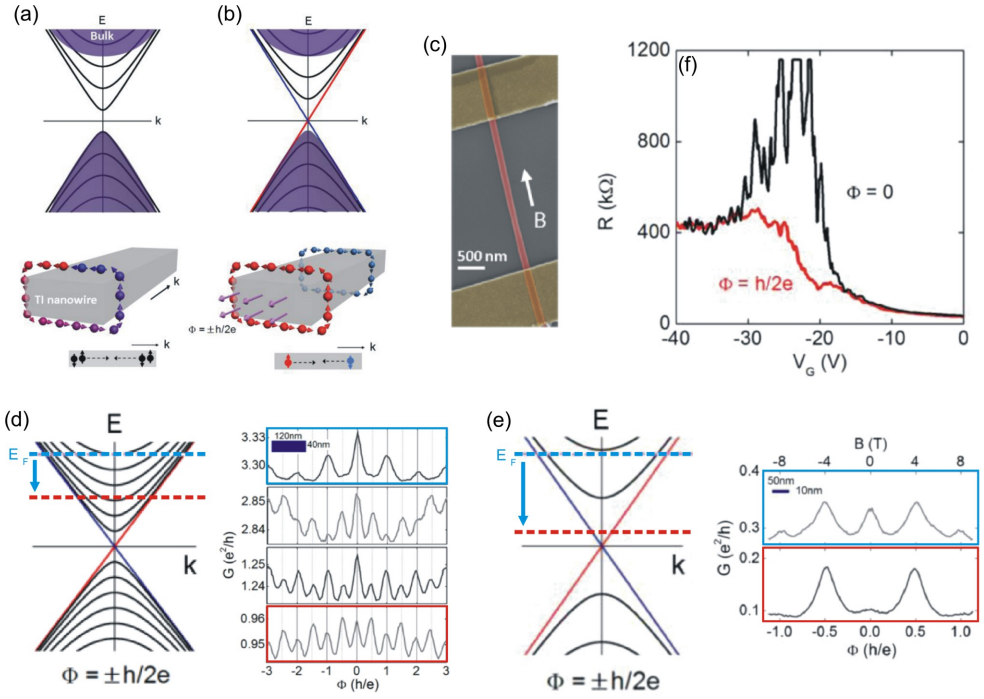

FIG. 15: (a) Top: band structure of a topological insulator nanowire in the absence of magnetic field. The black solid lines denote the discrete 1D subbands with spin degeneracy. Bottom: Cartoon illustrates additional π Berry's phase from a 2 π rotation of electrons (red to blue color transition). (b) Top: band structure of a topological insulator nanowire in a magnetic field corresponds to $\Phi = \pm h/2e$. The gapless bands (red and blue) is not spin degenerated and is referred as 1D helical mode. Bottom: The same as the cartoon in (a) but with $\Phi = \pm h/2e$ which results in helical 1D channels (blue and red). (c) A false-colored scanning electron microscope image of a Bi_2Se_3 core (40 nm height × 120 nm width) and an amorphous Se shell (2 nm) nanowire. (d) Left: Schematic band structure of 1D modes in TI nanowires of larger perimeter (L = 300 nm) with flux value $\Phi = \pm h/2e$. The location of Fermi level (E_F) is tuned by gating. Right: Magnetoconductance oscillations of the device shown in (c) at four different gate voltages (from top to bottom V_G= -40 V, -45 V, -85 V, -95 V). The color of rectangle is associated with the E_F on the left panel. (e) Left: Schematic band structure of 1D modes in TI nanowires of smaller perimeter (L = 100 nm) with quantum flux value $\Phi = \pm h/2e$. Right: Magnetoconductance of another nanowire device (10 nm height × 50 nm width) at V_G = -25 V (top) and V_G = -45 V (bottom). (f) Resistance (R) vs gate voltage (V_G) graph from a nanowire (10 nm height × 40 nm width), with Φ = 0 (black) and $\Phi = h/2e$ (red). Adapted with permission from ref. [5]. Copyright 2014 American Chemical Society.

4.2. Bi_2Se_3 quantum dots

A TI quantum dot is an interesting platform in which single electron transport may be spin polarized and can be used as a spin qubit. Fig. 16(a) shows an optical micrograph of a Bi_2Se_3 quantum dot device. A Bi_2Se_3 nanoribbon with a width of 200 nm and a thickness of 7 nm was mechanically exfoliated on Si/SiO_2 substrate. In order to create quantum confinement, parts of the Bi_2Se_3 nanoribbon were etched (by N_2 plasma) into a thin slab to induce a tunnel coupling between top and bottom surfaces, and thus open a band gap. Fig. 16(b) shows an AFM image of the nanoribbon after etching, where the etched region with a thickness of 3-5 QLs [inset in Fig. 16(b)] will be contacted by Cr/Au (2 nm/28 nm) electrodes. The etched Bi_2Se_3 thin films act as gate-tunable tunnel barriers, thus a quantum dot can be defined between two adjacent etched regions (i.e. between two electrodes) as shown in the inset of Fig. 16(a). Fig. 16(c) shows the differential conductance $G = dI/dV$ as a function of back-gate voltage V_g at zero source-drain bias $V_b = 0$ for the device shown in Fig. 16(a). The current pinch-off region at large negative V_g indicates the n-doped Bi_2Se_3 thin films are tuned at the band-gap, in which the transport is suppressed to a gap regime ($V_g \leq$-24 V). Within the transport gap, quasi-periodic narrow conductance peaks were observed, indicating the device is operating in the Coulomb blockade regime. This could be further confirmed by the Coulomb diamond measurements, where $G = dI/dV$ as a function of both V_g and V_b was shown in the inset of Fig. 16(c). The diamonds with charging energies E_C ranging from 5-10 meV suggest a variation in dot size, possibly due to the inevitable gate modulation of tunnel barriers. The smallest charging energy 5 meV corresponds to an effective dot radius r = 113 nm if the disc plate capacitance model $E_C = e^2/8\epsilon\epsilon_0 r$ is used, in agreement with the dimension of the dot A= $L \times W$= (200 × 200) nm^2. The excited states were re-

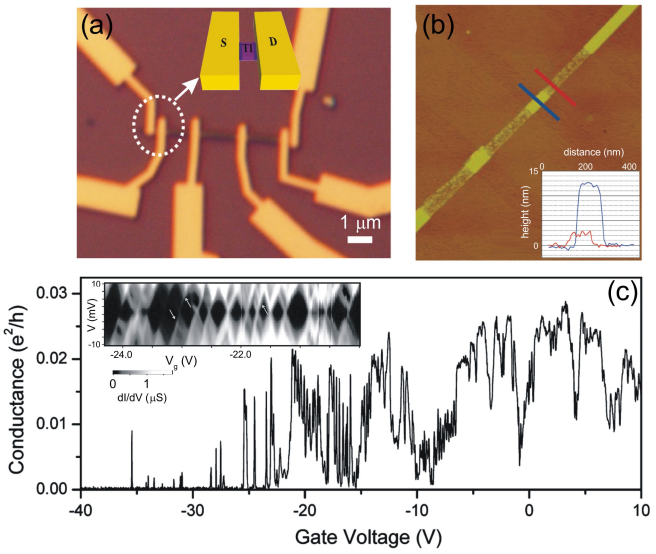

FIG. 16: (a) Optical micrograph of a 7 nm thick, mechanically exfoliated Bi_2Se_3 nanoribbon contacted by Cr/Au (2 nm/28 nm) contacts. Inset: Schematic of a Bi_2Se_3 quantum dot forms between two contacts. Dashed circle shows the device studied in ref. [4]. (b) Atomic force micrograph of a 12 nm thick nanoribbon after etching with PMMA mask. Inset: Line traces of topographic data along blue line (unetched area) and red line (etched area). (c) Gate voltage dependence of differential conductance ($G = dI/dV$) shows a current pinch-off regime with quasi-periodic narrow conductance peaks. Inset: Coulomb diamond measurements on the device. Arrows indicate the excited states of quantum dot energy levels. Adapted with permission from ref. [4]. Copyright 2012 American Chemical Society.

solved at the edges of the diamond at around 1 meV, as indicated by the arrows in the inset of Fig. 16(c). Although the spin-texture of surface states may enable TI quantum dots to be used as single-spin generators, non spin-polarized bulk contribution cannot be ruled out. Thus, future experiments are needed to detect spin polarization of charges through TI QDs.

5. SUMMARY AND PERSPECTIVE

In conclusion, we have given an overview of a number of electron transport experiments performed on nanostructures fabricated from both graphene and topological insulators. We described the basic transport properties of graphene nanodevices (GNRs, GSQDs and GDQDs) fabricated on SiO_2 at low temperature and high magnetic fields. For comparison, these devices on hBN substrate were also reviewed. GNRs fabricated on SiO_2 and hBN both show the presence of strongly localized states, but the origin of the former mainly comes from the substrate disorder while the latter can be attributed to the edge roughness if the edge-to-bulk ratio is large. GSQD fabricated on SiO_2 and hBN show a distinct difference in their Coulomb blockade peak-spacing fluctuations, indicating that edge roughness is the dominating source of disorder for QDs with diameters less than 100 nm. We have also described the power of pulsed gating to probe electron relaxation time in a GSQD and to generate frequency-dependent pumped current in a GDQD. We have also reviewed a few topological insulator nanodevices for their exotic topological surface states. The discrete 1D subbands of Bi_2Se_3 nanowire can be periodically modulated by a magnetic field applied along the nanowires length, resulting in the h/e periodicity in magnetooscillations whose amplitude is tunable by gate voltage. We have also reviewed the single electron tunneling can be manifested in a Bi_2Se_3 single quantum dot.

The absence of spin blockade in graphene double quantum dots [50, 51, 79–83] and the fact that the measured spin relaxation time in 2D graphene flakes is shorter than expected [84–88], suggesting there are extrinsic effects that govern the spin relaxation dynamics in graphene. These can be due to the scattering of electrons off magnetic impurities originating from vacancies of carbon atom or graphene edge roughness. Since all the reported GQDs used graphene constrictions as tunnel barriers, electron spin altered by the constriction edge during transport is inevitable. One possible solution to this problem is to use electrical-field induced band-gap in bilayer graphene to define the quantum dots [53, 54]. However, the small induced energy gap ($\approx$ 200 meV [143]) may limit the energy range available for quantum dot physics. Recently, a single quantum dot is also demonstrated in WSe2 using electrical gating [144]. The large band gap in WSe2 ($\approx$ 1.8 eV in monolayer) allows wide range of energy to be accessed in the QD. Nevertheless, gated DQD on both materials has not been reported so far as well as any spin related measurements. Another approach to reduce the edge effect is to use functionalized graphene, such as fluorinated graphene (FG), to define quantum confinement and passivate graphene edge at the same time. Nano-patterning of fluorinated graphene has been achieved by using scanning probe lithography and electron beam irradiation [41, 42]; in each case graphene nanochannels are surrounded by insulating FG to form constrictions. However, up to date GQDs defined by FG have not been reported.

Vertical tunneling to graphene quantum dot using hBN as tunnel barriers may also serve as a good solution to minimize the edge effect from graphene constrictions. The vertical GQD tunneling devices offer several advantages over their lateral counterparts. The tunneling can continue to happen even if the graphene bulk is in an insulating state (for example, at high B-field where Landau levels are formed), and is expected to provide better energy resolution as the B-field modulation on the GNR tunnel barriers is absent. Recently, a vertical stack of graphene nanoribbon and 2D graphene sheet (separated by a 13 nm thick hBN layer) has been reported, in which

Coulomb resonance of the GNR is used to probe the local density of state of the graphene sheet [145]. In addition, a stack of two graphene nanoribbon vertically separated by a 12 nm thick hBN layer has shown the capacitively coupled double-dot feature in the charge stability diagram [146]. However, vertical tunneling to graphene nanostructures through thin hBN as a tunnel barrier is still lacking. More efforts are needed to build and investigate the spin relaxation dynamics in such a system.

The spin-momentum locking nature of TI surface states offer the possibility of using TI quantum dot as single spin generator. To date, no experimental result has shown to detect the spin polarization in TI quantum dot transport. One potential challenge may lie in putting ferromagnetic contact to TI materials, which may require further experimental efforts in interface engineering. More sophisticated designs of the TI quantum dots are needed to study the controllability of confined charges as well as the spin-related transport properties.

6. ACKNOWLEDGMENTS

The authors would like to acknowledge Malcolm Connolly for helping with preparation of the manuscript and proof read.

[1] S. Schnez, Applied Physics Letters **94**, 012107 (2009), URL http://dx.doi.org/doi/10.1063/1.3064128.

[2] J. Guttinger, Applied Physics Letters **93**, 212102 (2008), URL http://dx.doi.org/doi/10.1063/1.3036419.

[3] J. Guttinger, C. Stampfer, F. Libisch, T. Frey, J. Burgdorfer, T. Ihn, and K. Ensslin, Phys. Rev. Lett. **103**, 046810 (2009), URL http://link.aps.org/doi/10.1103/PhysRevLett.103.046810.

[4] S. Cho, D. Kim, P. Syers, N. P. Butch, J. Paglione, and M. S. Fuhrer, Nano Letters **12**, 469 (2012), pMID: 22181853, http://dx.doi.org/10.1021/nl203851g, URL http://dx.doi.org/10.1021/nl203851g.

[5] S. S. Hong, Y. Zhang, J. J. Cha, X.-L. Qi, and Y. Cui, Nano Letters **14**, 2815 (2014), pMID: 24679125, http://dx.doi.org/10.1021/nl500822g, URL http://dx.doi.org/10.1021/nl500822g.

[6] Y. Li and N. Mason, ArXiv e-prints (2013), 1312.3939.

[7] R. Hanson, L. P. Kouwenhoven, J. R. Petta, S. Tarucha, and L. M. K. Vandersypen, Rev. Mod. Phys. **79**, 1217 (2007), URL http://link.aps.org/doi/10.1103/RevModPhys.79.1217.

[8] F. A. Zwanenburg, A. S. Dzurak, A. Morello, M. Y. Simmons, L. C. L. Hollenberg, G. Klimeck, S. Rogge, S. N. Coppersmith, and M. A. Eriksson, Rev. Mod. Phys. **85**, 961 (2013), URL http://link.aps.org/doi/10.1103/RevModPhys.85.961.

[9] K. S. Novoselov, A. K. Geim, S. V. Morozov, D. Jiang, Y. Zhang, S. V. Dubonos, I. V. Grigorieva, and A. A. Firsov, Science **306**, 666 (2004), URL http://www.sciencemag.org/content/306/5696/666.abstract.

[10] B. Trauzettel, D. V. Bulaev, D. Loss, and G. Burkard, Nat Phys **3**, 192 (2007), ISSN 1745-2473, URL http://dx.doi.org/10.1038/nphys544.

[11] A. K. Geim and I. V. Grigorieva, Nature **499**, 419 (2013), ISSN 0028-0836, URL http://dx.doi.org/10.1038/nature12385.

[12] D. R., Y. F., MericI., LeeC., WangL., SorgenfreiS., WatanabeK., TaniguchiT., KimP., S. L., et al., Nat Nano **5**, 722 (2010), ISSN 1748-3387, URL http://dx.doi.org/10.1038/nnano.2010.172.

[13] D. Golberg, Y. Bando, Y. Huang, T. Terao, M. Mitome, C. Tang, and C. Zhi, ACS Nano **4**, 2979 (2010), ISSN 1936-0851, URL http://dx.doi.org/10.1021/nn1006495.

[14] C. R. Dean, L. Wang, P. Maher, C. Forsythe, F. Ghahari, Y. Gao, J. Katoch, M. Ishigami, P. Moon, M. Koshino, et al., Nature **497**, 598 (2013), ISSN 0028-0836, URL http://dx.doi.org/10.1038/nature12186.

[15] L. A. Ponomarenko, R. V. Gorbachev, G. L. Yu, D. C. Elias, R. Jalil, A. A. Patel, A. Mishchenko, A. S. Mayorov, C. R. Woods, J. R. Wallbank, et al., Nature **497**, 594 (2013), ISSN 0028-0836, URL http://dx.doi.org/10.1038/nature12187.

[16] B. Hunt, J. D. Sanchez-Yamagishi, A. F. Young, M. Yankowitz, B. J. LeRoy, K. Watanabe, T. Taniguchi, P. Moon, M. Koshino, P. Jarillo-Herrero, et al., Science **340**, 1427 (2013), URL http://www.sciencemag.org/content/340/6139/1427.abstract.

[17] F. Amet, J. R. Williams, A. G. F. Garcia, M. Yankowitz, K. Watanabe, T. Taniguchi, and D. Goldhaber-Gordon, Phys. Rev. B **85**, 073405 (2012), URL http://link.aps.org/doi/10.1103/PhysRevB.85.073405.

[18] L. Britnell, R. V. Gorbachev, R. Jalil, B. D. Belle, F. Schedin, M. I. Katsnelson, L. Eaves, S. V. Morozov, A. S. Mayorov, N. M. R. Peres, et al., Nano Lett. **12**, 1707 (2012), ISSN 1530-6984, URL http://dx.doi.org/10.1021/nl3002205.

[19] L. Britnell, R. V. Gorbachev, R. Jalil, B. D. Belle, F. Schedin, A. Mishchenko, T. Georgiou, M. I. Katsnelson, L. Eaves, S. V. Morozov, et al., Science **335**, 947 (2012), URL http://www.sciencemag.org/content/335/6071/947.abstract.

[20] D. Kong and Y. Cui, Nat Chem **3**, 845 (2011), ISSN 1755-4330, URL http://dx.doi.org/10.1038/nchem.1171.

[21] J. J. Cha, K. J. Koski, and Y. Cui, Phys. Status Solidi RRL **7**, 15 (2013), ISSN 1862-6270, URL http://dx.doi.org/10.1002/pssr.201206393.

[22] M. Z. Hasan and C. L. Kane, Rev. Mod. Phys. **82**, 3045 (2010), URL http://link.aps.org/doi/10.1103/RevModPhys.82.3045.

[23] F. Molitor, A. Jacobsen, C. Stampfer, J. Guttinger, J.ttinger, T. Ihn, and K. Ensslin, Phys. Rev. B **79**, 075426 (2009), URL http://link.aps.org/doi/10.1103/PhysRevB.79.075426.

[24] C. Stampfer, J. Guttinger, S. Hellmuller, F. Molitor, K. Ensslin, and T. Ihn, Phys. Rev. Lett. **102**, 056403 (2009), URL http://link.aps.org/doi/10.1103/PhysRevLett.102.056403.

[25] A. H. Castro Neto, F. Guinea, N. M. R. Peres, K. S. Novoselov, and A. K. Geim, Rev. Mod. Phys. **81**, 109 (2009), URL http://link.aps.org/doi/10.1103/

RevModPhys.81.109.
[26] S. Das Sarma, S. Adam, E. H. Hwang, and E. Rossi, Rev. Mod. Phys. **83**, 407 (2011), URL http://link.aps.org/doi/10.1103/RevModPhys.83.407.
[27] M. I. Katsnelson, K. S. Novoselov, and A. K. Geim, Nat Phys **2**, 620 (2006), ISSN 1745-2473, URL http://dx.doi.org/10.1038/nphys384.
[28] A. F. Young and P. Kim, Nat Phys **5**, 222 (2009), ISSN 1745-2473, URL http://dx.doi.org/10.1038/nphys1198.
[29] N. Stander, B. Huard, and D. Goldhaber-Gordon, Phys. Rev. Lett. **102**, 026807 (2009), URL http://link.aps.org/doi/10.1103/PhysRevLett.102.026807.
[30] A. K. Geim and K. S. Novoselov, Nat Mater **6**, 183 (2007), ISSN 1476-1122, URL http://dx.doi.org/10.1038/nmat1849.
[31] Y.-M. Lin, V. Perebeinos, Z. Chen, and P. Avouris, Phys. Rev. B **78**, 161409 (2008), URL http://link.aps.org/doi/10.1103/PhysRevB.78.161409.
[32] C. Stampfer, S. Fringes, J. Guttinger, F. Molitor, C. Volk, B. Terrs, J. Dauber, S. Engels, S. Schnez, A. Jacobsen, et al., **6**, 271 (2011), ISSN 2095-0462, URL http://dx.doi.org/10.1007/s11467-011-0182-3.
[33] M. Y. Han, B. Ozyilmaz, Y. Zhang, and P. Kim, Phys. Rev. Lett. **98**, 206805 (2007), URL http://link.aps.org/doi/10.1103/PhysRevLett.98.206805.
[34] K. Todd, H.-T. Chou, S. Amasha, and D. Goldhaber-Gordon, Nano Lett. **9**, 416 (2008), ISSN 1530-6984, URL http://dx.doi.org/10.1021/nl803291b.
[35] J. Bai, R. Cheng, F. Xiu, L. Liao, M. Wang, A. Shailos, K. L. Wang, Y. Huang, and X. Duan, Nat Nano **5**, 655 (2010), ISSN 1748-3387, URL http://dx.doi.org/10.1038/nnano.2010.154.
[36] M. R. Connolly, K. L. Chiu, A. Lombardo, A. Fasoli, A. C. Ferrari, D. Anderson, G. A. C. Jones, and C. G. Smith, Phys. Rev. B **83**, 115441 (2011), URL http://link.aps.org/doi/10.1103/PhysRevB.83.115441.
[37] X. Wang, Y. Ouyang, L. Jiao, H. Wang, L. Xie, J. Wu, J. Guo, and H. Dai, Nat Nano **6**, 563 (2011), ISSN 1748-3387, URL http://dx.doi.org/10.1038/nnano.2011.138.
[38] L. Jiao, X. Wang, G. Diankov, H. Wang, and H. Dai, Nat Nano **5**, 321 (2010), ISSN 1748-3387, URL http://dx.doi.org/10.1038/nnano.2010.54.
[39] D. Wei, L. Xie, K. K. Lee, Z. Hu, S. Tan, W. Chen, C. H. Sow, K. Chen, Y. Liu, and A. T. S. Wee, Nat Commun **4**, 1374 (2013), URL http://dx.doi.org/10.1038/ncomms2366.
[40] X. Wang and H. Dai, Nat Chem **2**, 661 (2010), ISSN 1755-4330, URL http://dx.doi.org/10.1038/nchem.719.
[41] F. Withers, T. H. Bointon, M. Dubois, S. Russo, and M. F. Craciun, Nano Letters **11**, 3912 (2011), pMID: 21851114, http://dx.doi.org/10.1021/nl2020697, URL http://dx.doi.org/10.1021/nl2020697.
[42] W.-K. Lee, J. T. Robinson, D. Gunlycke, R. R. Stine, C. R. Tamanaha, W. P. King, and P. E. Sheehan, Nano Letters **11**, 5461 (2011), pMID: 22050117, http://dx.doi.org/10.1021/nl203225w, URL http://dx.doi.org/10.1021/nl203225w.
[43] A. Dorn, T. Ihn, K. Ensslin, W. Wegscheider, and M. Bichler, Phys. Rev. B **70**, 205306 (2004), URL http://link.aps.org/doi/10.1103/PhysRevB.70.205306.
[44] J. Guttinger, F. Molitor, C. Stampfer, S. Schnez, A. Jacobsen, S. Droscher, T. Ihn, and K. Ensslin, Reports on Progress in Physics **75**, 126502 (2012), ISSN 0034-4885, URL http://stacks.iop.org/0034-4885/75/i=12/a=126502.
[45] J. Martin, N. Akerman, G. Ulbricht, T. Lohmann, J. H. Smet, K. von Klitzing, and A. Yacoby, Nat Phys **4**, 144 (2008), ISSN 1745-2473, URL http://dx.doi.org/10.1038/nphys781.
[46] D. Bischoff, A. Varlet, P. Simonet, M. Eich, H. C. Overweg, T. Ihn, and K. Ensslin, Applied Physics Reviews **2**, 031301 (2015), URL http://scitation.aip.org/content/aip/journal/apr2/2/3/10.1063/1.4926448.
[47] C. Volk, C. Neumann, S. Kazarski, S. Fringes, S. Engels, F. Haupt, A. Muller, T.ller, and C. Stampfer, Nat Commun **4**, 1753 (2013), URL http://dx.doi.org/10.1038/ncomms2738.
[48] K. L. Chiu, M. R. Connolly, A. Cresti, C. Chua, S. J. Chorley, F. Sfigakis, S. Milana, A. C. Ferrari, J. P. Griffiths, G. A. C. Jones, et al., Phys. Rev. B **85**, 205452 (2012), URL http://link.aps.org/doi/10.1103/PhysRevB.85.205452.
[49] J. Guttinger, T. Frey, C. Stampfer, T. Ihn, and K. Ensslin, Phys. Rev. Lett. **105**, 116801 (2010), URL http://link.aps.org/doi/10.1103/PhysRevLett.105.116801.
[50] X. L. Liu, D. Hug, and L. M. K. Vandersypen, Nano Letters **10**, 1623 (2010), ISSN 1530-6984, URL http://dx.doi.org/10.1021/nl9040912.
[51] C. Volk, S. Fringes, B. Terres, J. Dauber, S. Engels, S. Trellenkamp, and C. Stampfer, Nano Letters **11**, 3581 (2011), ISSN 1530-6984, URL http://pubs.acs.org/doi/abs/10.1021/nl201295s.
[52] M. R. Connolly, K. L. Chiu, S. P. Giblin, M. Kataoka, J. D. Fletcher, C. Chua, J. P. Griffiths, G. A. C. Jones, V. I. Fal'ko, and C. G. S. T. J. B. M. Janssen, Nat Nano **8**, 417 (2013), ISSN 1748-3387, URL http://dx.doi.org/10.1038/nnano.2013.73.
[53] A. S. M. Goossens, S. C. M. Driessen, T. A. Baart, K. Watanabe, T. Taniguchi, and L. M. K. Vandersypen, Nano Lett. **12**, 4656 (2012), ISSN 1530-6984, URL http://dx.doi.org/10.1021/nl301986q.
[54] M. T. Allen, J. Martin, and A. Yacoby, Nat Commun **3**, 934 (2012), URL http://dx.doi.org/10.1038/ncomms1945.
[55] Y. Zhang, V. W. Brar, C. Girit, A. Zettl, and M. F. Crommie, Nat Phys **5**, 722 (2009), ISSN 1745-2473, URL http://dx.doi.org/10.1038/nphys1365.
[56] F. Amet, J. R. Williams, A. G. F. Garcia, M. Yankowitz, K. Watanabe, T. Taniguchi, and D. Goldhaber-Gordon, Phys. Rev. B **85**, 073405 (2012), URL http://link.aps.org/doi/10.1103/PhysRevB.85.073405.
[57] N. N. Klimov, S. Jung, S. Zhu, T. Li, C. A. Wright, S. D. Solares, D. B. Newell, N. B. Zhitenev, and J. A. Stroscio, Science **336**, 1557 (2012), http://www.sciencemag.org/content/336/6088/1557.full.pdf, URL http://www.sciencemag.org/content/336/6088/1557.abstract.
[58] F. Molitor, J. Guttinger, C. Stampfer, S. Druscher, A. Jacobsen, T. Ihn, and K. Ensslin, Journal of Physics: Condensed Matter **23**, 243201 (2011), ISSN 0953-8984, URL http://stacks.iop.org/0953-8984/23/i=24/a=243201.
[59] V. Fock, **47**, 446 (1928), ISSN 0044-3328, URL http://dx.doi.org/10.1007/BF01390750.

[60] L. P. Kouwenhoven, D. G. Austing, and S. Tarucha, Reports on Progress in Physics **64**, 701 (2001), ISSN 0034-4885, URL http://stacks.iop.org/0034-4885/64/i=6/a=201.

[61] S. Schnez, K. Ensslin, M. Sigrist, and T. Ihn, Phys. Rev. B **78**, 195427 (2008), URL http://link.aps.org/doi/10.1103/PhysRevB.78.195427.

[62] P. Recher, J. Nilsson, G. Burkard, and B. Trauzettel, Phys. Rev. B **79**, 085407 (2009), URL http://link.aps.org/doi/10.1103/PhysRevB.79.085407.

[63] J. A. Folk, C. M. Marcus, R. Berkovits, I. L. Kurland, I. L. Aleiner, and B. L. Altshuler, Physica Scripta **2001**, 26 (2001), ISSN 1402-4896, URL http://stacks.iop.org/1402-4896/2001/i=T90/a=003.

[64] S. Lindemann, T. Ihn, T. Heinzel, W. Zwerger, K. Ensslin, K. Maranowski, and A. C. Gossard, Phys. Rev. B **66**, 195314 (2002), URL http://link.aps.org/doi/10.1103/PhysRevB.66.195314.

[65] D. Goldhaber-Gordon, H. Shtrikman, D. Mahalu, D. Abusch-Magder, U. Meirav, and M. A. Kastner, Nature **391**, 156 (1998), ISSN 0028-0836, URL http://dx.doi.org/10.1038/34373.

[66] S. J. Chorley, G. Giavaras, J. Wabnig, G. A. C. Jones, C. G. Smith, G. A. D. Briggs, and M. R. Buitelaar, Phys. Rev. Lett. **106**, 206801 (2011), URL http://link.aps.org/doi/10.1103/PhysRevLett.106.206801.

[67] S. Droscher, J. Guttinger, T. Mathis, B. Batlogg, T. Ihn, and K. Ensslin, Applied Physics Letters **101**, 043107 (2012), URL http://scitation.aip.org/content/aip/journal/apl/101/4/10.1063/1.4737937.

[68] T. Fujisawa, Y. Tokura, and Y. Hirayama, Phys. Rev. B **63**, 081304 (2001), URL http://link.aps.org/doi/10.1103/PhysRevB.63.081304.

[69] T. Fujisawa, D. G. Austing, Y. Tokura, Y. Hirayama, and S. Tarucha, Nature **419**, 278 (2002), ISSN 0028-0836, URL http://dx.doi.org/10.1038/nature00976.

[70] T. Fujisawa, D. G. Austing, Y. Tokura, Y. Hirayama, and S. Tarucha, Phys. Rev. Lett. **88**, 236802 (2002), URL http://link.aps.org/doi/10.1103/PhysRevLett.88.236802.

[71] W. G. van der Wiel, S. De Franceschi, J. M. Elzerman, T. Fujisawa, S. Tarucha, and L. P. Kouwenhoven, Rev. Mod. Phys. **75**, 1 (2002), URL http://link.aps.org/doi/10.1103/RevModPhys.75.1.

[72] A. Pfund, I. Shorubalko, R. Leturcq, and K. Ensslin, Applied Physics Letters **89**, 252106 (2006), URL http://scitation.aip.org/content/aip/journal/apl/89/25/10.1063/1.2409625.

[73] M. D. Schroer, K. D. Petersson, M. Jung, and J. R. Petta, Phys. Rev. Lett. **107**, 176811 (2011), URL http://link.aps.org/doi/10.1103/PhysRevLett.107.176811.

[74] S. Pecker, F. Kuemmeth, A. Secchi, M. Rontani, D. C. Ralph, P. L. McEuen, and S. Ilani, Nat Phys **9**, 576 (2013), ISSN 1745-2473, URL http://dx.doi.org/10.1038/nphys2692.

[75] K. Ono, D. G. Austing, Y. Tokura, and S. Tarucha, Science **297**, 1313 (2002), URL http://www.sciencemag.org/content/297/5585/1313.abstract.

[76] A. C. Johnson, J. R. Petta, J. M. Taylor, A. Yacoby, M. D. Lukin, C. M. Marcus, M. P. Hanson, and A. C. Gossard, Nature **435**, 925 (2005), ISSN 0028-0836, URL http://dx.doi.org/10.1038/nature03815.

[77] A. C. Johnson, J. R. Petta, C. M. Marcus, M. P. Hanson, and A. C. Gossard, Phys. Rev. B **72**, 165308 (2005), URL http://link.aps.org/doi/10.1103/PhysRevB.72.165308.

[78] K. D. Petersson, C. G. Smith, D. Anderson, P. Atkinson, G. A. C. Jones, and D. A. Ritchie, Nano Lett. **10**, 2789 (2010), ISSN 1530-6984, URL http://dx.doi.org/10.1021/nl100663w.

[79] S. Moriyama, D. Tsuya, E. Watanabe, S. Uji, M. Shimizu, T. Mori, T. Yamaguchi, and K. Ishibashi, Nano Lett. **9**, 2891 (2009), ISSN 1530-6984, URL http://dx.doi.org/10.1021/nl9011535.

[80] F. Molitor, H. Knowles, S. Droscher, U. Gasser, T. Choi, P. Roulleau, J. Guttinger, A. Jacobsen, C. Stampfer, K. Ensslin, et al., EPL (Europhysics Letters) **89**, 67005 (2010), URL http://stacks.iop.org/0295-5075/89/i=6/a=67005.

[81] L.-J. Wang, H.-O. Li, T. Tu, G. Cao, C. Zhou, X.-J. Hao, Z. Su, M. Xiao, G.-C. Guo, A. M. Chang, et al., Applied Physics Letters **100**, 022106 (2012), URL http://scitation.aip.org/content/aip/journal/apl/100/2/10.1063/1.3676083.

[82] D. Wei, H.-O. Li, G. Cao, G. Luo, Z.-X. Zheng, T. Tu, M. Xiao, G.-C. Guo, H.-W. Jiang, and G.-P. Guo, Sci. Rep. **3**, (2013), URL http://dx.doi.org/10.1038/srep03175.

[83] K. L. Chiu, M. R. Connolly, A. Cresti, J. P. Griffiths, G. A. C. Jones, and C. G. Smith, ArXiv e-prints (2015), 1505.01885.

[84] N. Tombros, C. Jozsa, M. Popinciuc, H. T. Jonkman, and B. J. van Wees, Nature **448**, 571 (2007), ISSN 0028-0836, URL http://dx.doi.org/10.1038/nature06037.

[85] W. Han, K. Pi, K. M. McCreary, Y. Li, J. J. I. Wong, A. G. Swartz, and R. K. Kawakami, Phys. Rev. Lett. **105**, 167202 (2010), URL http://link.aps.org/doi/10.1103/PhysRevLett.105.167202.

[86] W. Han and R. K. Kawakami, Phys. Rev. Lett. **107**, 047207 (2011), URL http://link.aps.org/doi/10.1103/PhysRevLett.107.047207.

[87] T. Maassen, J. J. van den Berg, N. IJbema, F. Fromm, T. Seyller, R. Yakimova, and B. J. van Wees, Nano Lett. **12**, 1498 (2012), ISSN 1530-6984, URL http://dx.doi.org/10.1021/nl2042497.

[88] M. Drogeler, F. Volmer, M. Wolter, B. Terres, K. Watanabe, T. Taniguchi, G. Gntherodt, C. Stampfer, and B. Beschoten, Nano Lett. **14**, 6050 (2014), ISSN 1530-6984, URL http://dx.doi.org/10.1021/nl501278c.

[89] D. Kochan, M. Gmitra, and J. Fabian, Phys. Rev. Lett. **112**, 116602 (2014), URL http://link.aps.org/doi/10.1103/PhysRevLett.112.116602.

[90] D. V. Tuan, F. Ortmann, D. Soriano, S. O. Valenzuela, and S. Roche, Nat Phys **10**, 857 (2014), ISSN 1745-2473, URL http://dx.doi.org/10.1038/nphys3083.

[91] F. Molitor, Applied Physics Letters **94**, 222107 (2009), URL http://dx.doi.org/doi/10.1063/1.3148367.

[92] L. J. Geerligs, V. F. Anderegg, P. A. M. Holweg, J. E. Mooij, H. Pothier, D. Esteve, C. Urbina, and M. H. Devoret, Phys. Rev. Lett. **64**, 2691 (1990), URL http://link.aps.org/doi/10.1103/PhysRevLett.64.2691.

[93] L. P. Kouwenhoven, A. T. Johnson, N. C. van der Vaart, C. J. P. M. Harmans, and C. T. Foxon, Phys. Rev. Lett. **67**, 1626 (1991), URL http://link.aps.org/doi/10.

1103/PhysRevLett.67.1626.

[94] H. Pothier, P. Lafarge, C. Urbina, D. Esteve, and M. H. Devoret, EPL (Europhysics Letters) **17**, 249 (1992), URL http://stacks.iop.org/0295-5075/17/i=3/a=011.

[95] A. Fuhrer, C. Fasth, and L. Samuelson, Applied Physics Letters **91**, 052109 (2007), URL http://scitation.aip.org/content/aip/journal/apl/91/5/10.1063/1.2767197.

[96] S. J. Chorley, J. Frake, C. G. Smith, G. A. C. Jones, and M. R. Buitelaar, Applied Physics Letters **100**, 143104 (2012), URL http://scitation.aip.org/content/aip/journal/apl/100/14/10.1063/1.3700967.

[97] M. W. Keller, J. M. Martinis, N. M. Zimmerman, and A. H. Steinbach, Applied Physics Letters **69**, 1804 (1996), URL http://scitation.aip.org/content/aip/journal/apl/69/12/10.1063/1.117492.

[98] N. Levy, S. A. Burke, K. L. Meaker, M. Panlasigui, A. Zettl, F. Guinea, A. H. C. Neto, and M. F. Crommie, Science **329**, 544 (2010), URL http://www.sciencemag.org/content/329/5991/544.abstract.

[99] A. A. Pacheco Sanjuan, Z. Wang, H. P. Imani, M. Vanevic, and S. Barraza-Lopez, Phys. Rev. B **89**, 121403 (2014), URL http://link.aps.org/doi/10.1103/PhysRevB.89.121403.

[100] S. Barraza-Lopez, A. A. Pacheco Sanjuan, Z. Wang, and M. Vanevic, Solid State Communications **166**, 70 (2013), ISSN 0038-1098, URL http://www.sciencedirect.com/science/article/pii/S0038109813002287.

[101] A. Muller, B. Kaestner, F. Hohls, T. Weimann, K. Pierz, and H. W. Schumacher, Journal of Applied Physics **115**, 233710 (2014), URL http://scitation.aip.org/content/aip/journal/jap/115/23/10.1063/1.4884617.

[102] S. Fringes, C. Volk, B. Terres, J. Dauber, S. Engels, S. Trellenkamp, and C. Stampfer, Phys. Status Solidi C **9**, 169 (2012), ISSN 1610-1642, URL http://dx.doi.org/10.1002/pssc.201100340.

[103] P. Roulleau, S. Baer, T. Choi, F. Molitor, J. Guttinger, T. Muller, S. Droscher, K. Ensslin, and T. Ihn, Nat Commun **2**, 239 (2011), URL http://dx.doi.org/10.1038/ncomms1241.

[104] K. L. Chiu, M. R. Connolly, A. Cresti, J. P. Griffiths, G. A. C. Jones, and C. G. Smith, Phys. Rev. B **92**, 155408 (2015), URL http://link.aps.org/doi/10.1103/PhysRevB.92.155408.

[105] M. Xu, T. Liang, M. Shi, and H. Chen, Chem. Rev. **113**, 3766 (2013), ISSN 0009-2665, URL http://dx.doi.org/10.1021/cr300263a.

[106] H. Wang, F. Liu, W. Fu, Z. Fang, W. Zhou, and Z. Liu, Nanoscale **6**, 12250 (2014), ISSN 2040-3364, URL http://dx.doi.org/10.1039/C4NR03435J.

[107] A. C. Ferrari, F. Bonaccorso, V. Fal'ko, K. S. Novoselov, S. Roche, P. Boggild, S. Borini, F. H. L. Koppens, V. Palermo, N. Pugno, et al., Nanoscale **7**, 4598 (2015), ISSN 2040-3364, URL http://dx.doi.org/10.1039/C4NR01600A.

[108] J. Xue, J. Sanchez-Yamagishi, D. Bulmash, P. Jacquod, A. Deshpande, K. Watanabe, T. Taniguchi, P. Jarillo-Herrero, and B. J. LeRoy, Nat Mater **10**, 282 (2011), ISSN 1476-1122, URL http://dx.doi.org/10.1038/nmat2968.

[109] F. Amet, A. J. Bestwick, J. R. Williams, L. Balicas, K. Watanabe, T. Taniguchi, and D. Goldhaber-Gordon, Nat Commun **6**, (2015), URL http://dx.doi.org/10.1038/ncomms6838.

[110] A. S. Mayorov, R. V. Gorbachev, S. V. Morozov, L. Britnell, R. Jalil, L. A. Ponomarenko, P. Blake, K. S. Novoselov, K. Watanabe, T. Taniguchi, et al., Nano Lett. **11**, 2396 (2011), ISSN 1530-6984, URL http://dx.doi.org/10.1021/nl200758b.

[111] S. J. Haigh, A. Gholinia, R. Jalil, S. Romani, L. Britnell, D. C. Elias, K. S. Novoselov, L. A. Ponomarenko, A. K. Geim, and R. Gorbachev, Nat Mater **11**, 764 (2012), ISSN 1476-1122, URL http://dx.doi.org/10.1038/nmat3386.

[112] L. Wang, I. Meric, P. Y. Huang, Q. Gao, Y. Gao, H. Tran, T. Taniguchi, K. Watanabe, L. M. Campos, D. A. Muller, et al., Science **342**, 614 (2013), URL http://www.sciencemag.org/content/342/6158/614.abstract.

[113] M. Yankowitz, J. Xue, D. Cormode, J. D. Sanchez-Yamagishi, K. Watanabe, T. Taniguchi, P. Jarillo-Herrero, P. Jacquod, and B. J. LeRoy, Nat Phys **8**, 382 (2012), ISSN 1745-2473, URL http://dx.doi.org/10.1038/nphys2272.

[114] D. Bischoff, T. Krhenmann, S. Drscher, M. A. Gruner, C. Barraud, T. Ihn, and K. Ensslin, Applied Physics Letters **101**, 203103 (2012), URL http://scitation.aip.org/content/aip/journal/apl/101/20/10.1063/1.4765345.

[115] D. Bischoff, F. Libisch, J. Burgdörfer, T. Ihn, and K. Ensslin, Phys. Rev. B **90**, 115405 (2014), URL http://link.aps.org/doi/10.1103/PhysRevB.90.115405.

[116] S. Engels, A. Epping, C. Volk, S. Korte, B. Voigtlander, K. Watanabe, T. Taniguchi, S. Trellenkamp, and C. Stampfer, Applied Physics Letters **103**, 073113 (2013), URL http://scitation.aip.org/content/aip/journal/apl/103/7/10.1063/1.4818627.

[117] A. Epping, S. Engels, C. Volk, K. Watanabe, T. Taniguchi, S. Trellenkamp, and C. Stampfer, Phys. Status Solidi B **250**, 2692 (2013), ISSN 1521-3951, URL http://dx.doi.org/10.1002/pssb.201300295.

[118] M. Konig, S. Wiedmann, C. Brne, A. Roth, H. Buhmann, L. W. Molenkamp, X.-L. Qi, and S.-C. Zhang, Science **318**, 766 (2007), URL http://www.sciencemag.org/content/318/5851/766.abstract.

[119] L. Fu, C. L. Kane, and E. J. Mele, Phys. Rev. Lett. **98**, 106803 (2007), URL http://link.aps.org/doi/10.1103/PhysRevLett.98.106803.

[120] J. E. Moore and L. Balents, Phys. Rev. B **75**, 121306 (2007), URL http://link.aps.org/doi/10.1103/PhysRevB.75.121306.

[121] R. Roy, Phys. Rev. B **79**, 195322 (2009), URL http://link.aps.org/doi/10.1103/PhysRevB.79.195322.

[122] D. Hsieh, D. Qian, L. Wray, Y. Xia, Y. S. Hor, R. J. Cava, and M. Z. Hasan, Nature **452**, 970 (2008), ISSN 0028-0836, URL http://dx.doi.org/10.1038/nature06843.

[123] Y. Xia, D. Qian, D. Hsieh, L. Wray, A. Pal, H. Lin, A. Bansil, D. Grauer, Y. S. Hor, R. J. Cava, et al., Nat Phys **5**, 398 (2009), ISSN 1745-2473, URL http://dx.doi.org/10.1038/nphys1274.

[124] G. Zhang, H. Qin, J. Teng, J. Guo, Q. Guo, X. Dai, Z. Fang, and K. Wu, Applied Physics Letters **95**, 053114 (2009), URL http://scitation.aip.org/content/aip/journal/apl/95/5/10.1063/1.3200237.

[125] J. G. Checkelsky, Y. S. Hor, R. J. Cava, and N. P. Ong, Phys. Rev. Lett. **106**, 196801 (2011), URL http://link.aps.org/doi/10.1103/PhysRevLett.106.196801.

[126] Y. Zhang, K. He, C.-Z. Chang, C.-L. Song, L.-L. Wang, X. Chen, J.-F. Jia, Z. Fang, X. Dai, W.-Y. Shan, et al., Nat Phys **6**, 584 (2010), ISSN 1745-2473, URL http://dx.doi.org/10.1038/nphys1689.

[127] I. Zutic, J. Fabian, and S. Das Sarma, Rev. Mod. Phys. **76**, 323 (2004), URL http://link.aps.org/doi/10.1103/RevModPhys.76.323.

[128] C. Nayak, S. H. Simon, A. Stern, M. Freedman, and S. Das Sarma, Rev. Mod. Phys. **80**, 1083 (2008), URL http://link.aps.org/doi/10.1103/RevModPhys.80.1083.

[129] J. Moore, Nat Phys **5**, 378 (2009), ISSN 1745-2473, URL http://dx.doi.org/10.1038/nphys1294.

[130] J. H. Bardarson, P. W. Brouwer, and J. E. Moore, Phys. Rev. Lett. **105**, 156803 (2010), URL http://link.aps.org/doi/10.1103/PhysRevLett.105.156803.

[131] Y. Zhang and A. Vishwanath, Phys. Rev. Lett. **105**, 206601 (2010), URL http://link.aps.org/doi/10.1103/PhysRevLett.105.206601.

[132] A. R. Akhmerov, J. Nilsson, and C. W. J. Beenakker, Phys. Rev. Lett. **102**, 216404 (2009), URL http://link.aps.org/doi/10.1103/PhysRevLett.102.216404.

[133] S. De Franceschi, L. Kouwenhoven, C. Schonenberger, and W. Wernsdorfer, Nat Nano **5**, 703 (2010), ISSN 1748-3387, URL http://dx.doi.org/10.1038/nnano.2010.173.

[134] J. E. Moore, Nature **464**, 194 (2010), ISSN 0028-0836, URL http://dx.doi.org/10.1038/nature08916.

[135] S. Cho, N. P. Butch, J. Paglione, and M. S. Fuhrer, Nano Lett. **11**, 1925 (2011), ISSN 1530-6984, URL http://dx.doi.org/10.1021/nl200017f.

[136] L. Fu and C. L. Kane, Phys. Rev. Lett. **100**, 096407 (2008), URL http://link.aps.org/doi/10.1103/PhysRevLett.100.096407.

[137] X.-L. Qi, T. L. Hughes, and S.-C. Zhang, Phys. Rev. B **78**, 195424 (2008), URL http://link.aps.org/doi/10.1103/PhysRevB.78.195424.

[138] H. Ji, J. M. Allred, N. Ni, J. Tao, M. Neupane, A. Wray, S. Xu, M. Z. Hasan, and R. J. Cava, Phys. Rev. B **85**, 165313 (2012), URL http://link.aps.org/doi/10.1103/PhysRevB.85.165313.

[139] P. Wei, F. Katmis, B. A. Assaf, H. Steinberg, P. Jarillo-Herrero, D. Heiman, and J. S. Moodera, Phys. Rev. Lett. **110**, 186807 (2013), URL http://link.aps.org/doi/10.1103/PhysRevLett.110.186807.

[140] D. Kong, J. C. Randel, H. Peng, J. J. Cha, S. Meister, K. Lai, Y. Chen, Z.-X. Shen, H. C. Manoharan, and Y. Cui, Nano Lett. **10**, 329 (2010), ISSN 1530-6984, URL http://dx.doi.org/10.1021/nl903663a.

[141] H. Peng, K. Lai, D. Kong, S. Meister, Y. Chen, X.-L. Qi, S.-C. Zhang, Z.-X. Shen, and Y. Cui, Nat Mater **9**, 225 (2010), ISSN 1476-1122, URL http://dx.doi.org/10.1038/nmat2609.

[142] S. S. Hong, W. Kundhikanjana, J. J. Cha, K. Lai, D. Kong, S. Meister, M. A. Kelly, Z.-X. Shen, and Y. Cui, Nano Lett. **10**, 3118 (2010), ISSN 1530-6984, URL http://dx.doi.org/10.1021/nl101884h.

[143] Y. Zhang, T.-T. Tang, C. Girit, Z. Hao, M. C. Martin, A. Zettl, M. F. Crommie, Y. R. Shen, and F. Wang, Nature **459**, 820 (2009), ISSN 0028-0836, URL http://dx.doi.org/10.1038/nature08105.

[144] X.-X. Song, D. Liu, V. Mosallanejad, J. You, T.-Y. Han, D.-T. Chen, H.-O. Li, G. Cao, M. Xiao, G.-C. Guo, et al., Nanoscale **7**, 16867 (2015), URL http://dx.doi.org/10.1039/C5NR04961J.

[145] D. Bischoff, M. Eich, A. Varlet, P. Simonet, T. Ihn, and K. Ensslin, Phys. Rev. B **91**, 115441 (2015), URL http://link.aps.org/doi/10.1103/PhysRevB.91.115441.

[146] D. Bischoff, M. Eich, O. Zilberberg, C. Rssler, T. Ihn, and K. Ensslin, Nano Lett. **15**, 6003 (2015), ISSN 1530-6984, URL http://dx.doi.org/10.1021/acs.nanolett.5b02167.